

Electronic and optical properties of two-dimensional materials consisting of group VI elements

André Mendes Marinho

Uminho | 2025

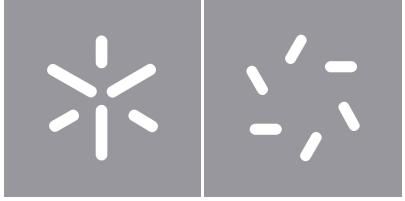


University of Minho
School of sciences

André Mendes Marinho

Electronic and optical properties of two-dimensional materials consisting of group VI elements

october 2025



University of Minho
School of Sciences

André Mendes Marinho

Electronic and optical properties of two-dimensional materials consisting of group VI elements

Master's Thesis in Physics

Thesis supervised by
Doctor Ricardo Mendes Ribeiro
Doctor Nuno M. R. Peres

october 2025

Copyright and Terms of Use for Third Party Work

This thesis reports on academic work that can be used by third parties as long as the internationally accepted standards and good practices are respected concerning copyright and related rights.

This work can thereafter be used under the terms established in the license below.

Readers needing authorization conditions not provided for in the indicated licensing should contact the author through the RepositóriUM of the University of Minho.

License granted to users of this work:



CC BY

https://creativecommons.org/licenses/by/4.0/

Acknowledgements

I am grateful to my supervisors, Doctor Ricardo Mendes Ribeiro and Doctor Nuno M.R. Peres, for presenting me with the opportunity of this research topic, and for guiding me throughout the work we did. I thank them for the many hours we shared nurturing my knowledge in physics, as well as for their empathy when personal challenges impacted my work. I take with me the example they set as researchers and human beings, which I know will help me in future endeavours. I would also like to thank Doctor António Costa for his assistance and availability. Furthermore, I am indebted to all the professors who have ever taught me, be it about advanced quantum mechanics or on how to count until ten, as the combination of their efforts is what allowed me to reach this level of education.

On a more personal note, I thank my parents for the sweat they shed to give me the possibility of attending university, something they never had access to. I thank my brother and my friends for the good times I shared with them during this period of my life. Finally, I am extremely thankful to my girlfriend, Laura, for being my "study buddy", for always supporting and encouraging me, and for her unconditional love and affection. Without her, this already rocky path would have become unbearable.

We gratefully acknowledge support by the Portuguese Foundation for Science and Technology (FCT) in the framework of the Strategic Funding UIDB/04650/2020, UIDB/50007/2020 and Associate Laboratory LA/P/0016/2020 and COMPETE 2020, PORTUGAL 2020, FEDER and through grant PTDC/FIS-MAC/2045/2021.



Statement of Integrity

I hereby declare having conducted this academic work with integrity.

I confirm that I have not used plagiarism or any form of undue use of information or falsification of results along the process leading to its elaboration.

I further declare that I have fully acknowledged the Code of Ethical Conduct of the University of Minho.

University of Minho, Braga, october 2025

André Mendes Marinho

Assinado por: **André Mendes Marinho**
Num. de Identificação: 14998800
Data: 2025.10.21 18:19:19+01'00'

Abstract

Group VI elemental 2D materials have been predicted to possess promising properties in electronics, optoelectronics, thermoelectricity, sensors, and detectors[1–5]. In this thesis, we present the electronic and optical properties of square selenene (s-Se), a 2D allotrope of selenium. We start by calculating the electronic properties using Density Functional Theory (DFT). These *ab initio* calculations show the formation of an anisotropic cone with semi-Dirac dispersion in a non-symmetric point, denoted P_1, in the Brillouin zone, which forms a narrow gap ($\sim$0.1 eV) due to spin-orbit coupling (SOC). Then, we uncover an intricate reciprocal space spin texture along the Brillouin zone, with spin-momentum locking around P_1. To conclude the DFT calculations, we show the existence of edge states in two types of s-Se nanoribbons, with one of them presenting topologically non-trivial features, which are confirmed in other works[1,6]. We then replicate a $k{\cdot}p$ Hamiltonian, for the band structure around P_1, from the literature[1] and add various SOC terms to obtain an effective model that describes the band structure data from fully relativistic DFT calculations and qualitatively reproduces the spin texture in reciprocal space. Using this effective model, we describe the exciton formation in the Dirac-like cone gap using the variational method while considering an anisotropic version of the Rytova-Keldysh potential[7]. This analysis provides a first characterisation of the exciton ground-state in square selenene, describing its binding energy (E_b=-24 meV) and wavefunction, which, to the best of our knowledge, have not been previously reported.

Keywords 2D elemental materials, density functional theory calculations, semi-Dirac materials, edge states, effective Hamiltonian, excitons, variational method, anisotropy effects

Resumo

Está previsto que materiais elementares bidimensionais (2D) do Grupo VI possuam propriedades promissoras para aplicações em eletrónica, optoeletrónica, termoeletricidade, sensores e detetores[1–5]. Nesta dissertação, apresentamos as propriedades eletrónicas e óticas do seleneno quadrado (s-Se), um alótropo bidimensional de selénio. Iniciamos com o cálculo das propriedades eletrónicas através de *Density Functional Theory* (DFT). Estes métodos *ab initio* revelam a formação de um semi cone de Dirac anisotrópico num ponto não simétrico, denotado P_1, da primeira zona de Brillouin, o qual abre num *gap* ($\sim$0.1 eV) devido a efeitos de acoplamento spin-órbita. Posteriormente, obtivemos uma textura de spin complexa no espaço recíproco, com *spin-momentum locking* a volta do ponto P_1. Para concluir os cálculos de DFT, demonstramos a existência de estados de borda em dois tipos de nanofitas, sendo que uma delas apresenta características toplógicas não triviais, confirmadas em outros estudos[1,6]. De seguida, replicamos um Hamiltoniano $k{\cdot}p$ a partir da literatura[1] , ao qual adicionámos diversos termos de acoplamento spin-órbita para descrever a estrutura de bandas relativista a volta de P_1, assim como replicar a textura de spin qualitativamente. Com base neste modelo efetivo, descrevemos a formação de excitões no *gap* do cone de Dirac, recorrendo ao método variacional e considerando uma versão anisotrópica do potencial de Rytova-Keldysh[7]. Esta análise permite a caracterização do estado excitónico fundamental no seleneno quadrado, com a determinação da sua energia de ligação (E_b = -24 meV) e da respetiva função de onda. Até ao presente, não há, segundo o nosso conhecimento, registo destes resultados na literatura científica.

Palavras-chave Materiais elementares bidimensionais, *Density Functional Theory*, estados de borda, Hamiltoniano efetivo, excitões, método variacional, efeitos de anisotropia

Contents

1 Introduction **1**

1.1 Group VI bulk materials . . . 1

1.2 2D selenium allotropes . . . 2

1.3 Square selenene . . . 2

1.4 Excitons . . . 3

1.5 Thesis layout . . . 4

2 Density Functional Theory **6**

2.1 Crystal Structure . . . 6

2.2 Convergence and structure optimisation . . . 7

2.3 Band structure . . . 8

2.4 Spin texture . . . 11

2.5 Edge states . . . 14

3 Effective Model **17**

3.1 $k{\cdot}p$ Hamiltonian . . . 17

3.2 Spin-orbit model . . . 19

3.3 Effective Masses . . . 24

3.4 Effective Screening Lengths . . . 25

4 Excitons **27**

4.1 Interaction energy approximation . . . 28

4.1.1 Radial term . . . 29

4.1.2 Angular term . . . 31

4.2 Energy functional . . . 34

4.2.1 Kinetic terms . . . 34

4.2.2 Potential term 35
4.2.3 Final energy functional 38

5 Conclusion, Limitations and Further Work 43

I Appendices 53

A PAOFLOW 54

B Effective Model: Anisotropic Rashba spin-orbit coupling term 56

C Anisotropic Poisson equation 58

List of Figures

1 Spatial configuration of square selenene. (a) Top and side view. (b) Perspective view. (c) 1st Brillouin zone of s-Se with high symmetry points. 7

2 Total energy convergence with respect to: (a) Kohn-Sham states energy cut-off, (b) Monkhorst-Pack grid size ($N \times N \times 1$). 8

3 Band structure of square selenene obtained from DFT, for non- and fully relativistic calculations, on a path between high symmetry points in the 1st Brillouin zone. The energy reference is set as the energy of the Dirac cone-like structure at P_1. 9

4 Band structure of square selenene obtained from DFT, for non- and fully relativistic calculations, around P_1 for the parallel ($q_{||}$) and perpendicular directions ($q_{\perp}$). Both graphs use the same scale to allow for direct comparison. 10

5 Valence and conduction band along the 1st Brillouin zone: (a) contour plots of the conduction (top) and valence (bottom) bands, (b) perspective render. 10

6 Spin texture of square selenene, constructed through the expected values of the spin operators - $\langle S_i \rangle$ - obtained from DFT along the entire 1st BZ. The arrows represent the *x* and *y* components, while the *z* component is represented using a colour scale. 12

7 Spin texture of square selenene, constructed through the expected values of the spin operators - $\langle S_i \rangle$ - obtained from DFT along the first quadrant of the 1st BZ. The arrows represent the *x* and *y* components, while the *z* component is represented using a colour scale. 13

8 (a) Rotated and scaled cell of square selenene. s-Se nanoribbon with a supercell, built from 3 new cells, to form : (b) a zigzag cut and (c) an armchair cut. The name of the cuts alludes to the shape of the nanoribbon's edge along the periodic direction, which is highlighted in blue. 14

9 (a) Electronic band structure of a square selenene zigzag nanoribbon with a width of ≈10 nm. (b) Collapsed contribution to the charge density of the states located at the vertical grey dashed line, for different bands. The colour bar is in units of e/a_0^3, while the bands and the collapsed contribution to the charge density are colour coded to indicate correspondence. 15

10 (a) Electronic band structure of a square selenene armchair nanoribbon with a width of ≈10 nm. (b) Collapsed contribution to the charge density of the states located at the vertical grey dashed line, for different bands. The colour bar is in units of e/a_0^3, while the bands and the collapsed contribution to the charge density are colour coded to indicate correspondence. 15

11 Contour plots of the valence (left) and conduction (right) bands that form the semi-Dirac cone near P_1, obtained from NR DFT calculations (solid black lines) and compared to the fitted $k{\cdot}p$ model (dashed coloured lines). 18

12 Bandgap along the main directions obtained from FR DFT calculations (black lines) compared to the fitted effective model (coloured dashed lines). 21

13 Bandgap along the main directions obtained from FR DFT calculations (black lines) compared to the fitted effective model, when Δ_{SO}=0 (dash-dotted blue lines) and $\alpha_R^{xy} = \alpha_R^{yx} = 0$ (dashed fuchsia lines). 21

14 Spin texture of the bands near P_1 obtained from FR DFT calculations. The arrows represent the x- and y-components of $\langle S_i \rangle$, while the colours represent the z-component. . . . 22

15 Spin texture of the bands near P_1 obtained from our effective model (with H_{S_z}). The arrows represent the *x*- and *y*- components of $\langle S_i \rangle$, while the colours represent the *z*-component. 23

16 Stylised illustration of an exciton in square selenene 27

17 Exact (black line) vs approximation (coloured dashed line) of the function f(q) with relative percentage error (grey line). The curves were calculated using $r_{0\parallel}$= 1691.08 Å and $r_{0\perp}$= 455.25 Å. 30

18 Numerical (black line) vs approximation (coloured dashed line) of $V_r(r)$ with relative percentage error (grey line). The curves where calculated using $r_{0\parallel}$= 1691.08 Å and $r_{0\perp}$= 455.25 Å. 31

19 Numerical (black lines) vs approximation (dashed coloured lines) of $V_\theta(r,\theta)$ for different angles (4 left panels), relative percentage error (large right panel: coloured lines) and decay lines of the square modulus of the trial wavefunction renormalised to 100 (large right panel: dash-dotted coloured lines). 32

20 Numerical (black lines) vs approximation (dashed coloured lines) of $V_{\bullet\bullet}(r,\theta)$ for different angles (4 left panels), relative percentage error (large right panel: coloured lines) and decay lines of the square modulus of the trial wavefunction renormalised to 100 (large right panel: dash-dotted coloured lines). 33

21 Compilation of exciton binding energies and band gaps of various 2D semiconductors, from different works. 40

22 Square modulus of the ground state excitonic wavefunction in square selenene, obtained using the effective masses from: (a) PAOFLOW, (b) Lin *et al.*[8]. The white dashed lines represent ellipses whose semi-major and semi-minor axes are the characteristic lengths L_j, which are the root-mean-square radius of the excitonic wavefunction. 42

23 Comparison of the band structures obtained from DFT (fully-relativistic), and PAOFLOW's real space Hamiltonian. 55

24 (a) Eigenvalues of the Rashba Hamiltonian in function of the Rashba parameter α_R.(b) Number of distinct eigenvalues of the anisotropic Rashba Hamiltonian in terms of the Rashba parameters α_R^{xy} and α_R^{yx}. 56

List of Tables

1 Structural parameters of square selenene 7

2 Converged parameters for DFT runs of the Kohn-Sham states energy cut-off and the size of the Monkhorst-Pack grid ($N \times N \times 1$). 8

3 Fitted parameters of the k·p Hamiltonian. 19

4 Fitted parameters of the effective model, with and without H_{Sz}. 20

5 Effective masses for holes and electrons along the along the $\|$- and $\perp$- direction in terms of the electron mass m_0 derived from the effective model 24

6 Effective screening lengths of square selenene along the $\|$- and $\perp$- direction obtained from our effective model. 26

7 Variational parameters ($\lambda_{\|}, \lambda_{\perp}$) of the trial excitonic wavefunction that minimise the energy functional for three different sets of effective masses. The resulting energies ($E_{\bullet}$) are decomposed into kinetic (T), radial (E_r) and angular contributions (E_θ). 39

8 Characteristic lengths of excitons in square selenene (source of the effective masses in parentheses), phosphorene, and InSb (3D). a_x is the excitonic Bohr radius. 42

Chapter 1

Introduction

In 2004, the Geim-Novoselov group, based at the University of Manchester, UK, launched what can be called the graphene golden era when they published a paper on its mechanical exfoliation from graphite[9], which would later earn them the 2010 Physics Nobel Prize. This event would cause quite a stir in the scientific community due to graphene's promising properties, such as remarkably high carrier mobilities at room temperature[9], Klein tunneling[10], and the highest ideal tensile strength[11,12]. It would also stimulate the research on two-dimensional materials beyond graphene, allowing for the emergence of multiple systems with equally interesting properties, such as transition metal dichalcogenides (TMDs)[13], Xenes[14], MXenes[15], and hexagonal boron nitride (hBN)[16].

1.1 Group VI bulk materials

Elements in the sixth group of the periodic table are known as chalcogens and among them two stand out as semiconductor materials: tellurium (Te) and selenium (Se)[1]. In their bulk form, both consist of atomic helical chains organised in a hexagonal pattern due to Van der Waals (VdW) forces[17]. The helical structure of the atomic chains makes them chiral crystals[18,19]. They both possess interesting properties, such as thermoelectricity[20], piezoelectricity[21–24] and photoconductivity[25,26]. Tellurium's primary technological application is as one of the three major types of thin-film solar cells, which accounted for 60% of tellurium utilisation worldwide in 2024, in the form of cadmium telluride (CdTe). This type accounted for 48% of all thin-film solar cells as of 2018[27]. Although the largest part of selenium usage is destined for agricultural purposes (40%), one fifth of it is employed in electronic and photoelectronic applications, one of them being in direct flat-panel X-ray detectors, where it is used as a photoconductor[27]. Due to its historical importance, we note that selenium was used as a photoabsorbing layer in the first solid-state solar cell,

[1] It is interesting to note that tellurium was named from the latin word "tellus", which means earth, ground or soil but also refers to Tellus, the goddess of the Earth in Roman mythology. Selenium is named after the Greek goddess of the moon, "Selene", in analogy to Tellurium due to their similarities, giving the pair a poetic naming convention.

created in 1876 by William Grylls Adams and Richard Evans Day, with an efficiency of 0.5%[28,29].

1.2 2D selenium allotropes

Monolayer selenium can exist in different phases: c-Se, t-Se, and s-Se, which were predicted as stable structures by Liu *et al.*[30].

c-Se is formed by a plane of parallel atomic helical chains connected by VdW forces. This allotrope has an indirect bandgap of 1.73 eV, which is hardly altered when considering spin-orbit coupling (SOC) effects, making it a semiconductor. Calculations with the Heyd–Scuseria–Ernzerhof (HSE)[31] functional increase this gap to 2.64 eV, and to 2.57 eV when using HSE+SOC. The carrier mobility of c-Se is strongly anisotropic[32], with values (in units of 10^3 $cm^2V^{-1}s^{-1}$) of 0.018 and 0.082 for electrons in the *x* and *y* directions and values of 0.571 and 0.112 for holes in the *x* and *y* directions, at room temperature. This gives factors[2] of approximately 4.55 and 5.1 for electrons and holes, respectively. For comparison, in single-layer black phosphorus, the same anisotropy factors for carrier mobility can reach approximately 6.4 and 2 for electrons and holes at 300K[33], depending on the carrier density. In their work, Qin *et al.*[34] measured the intrinsic hole mobility to be 0.26 10^3 $cm^2V^{-1}s^{-1}$ in 2D nanosheets of Se at 300K, with a minimum thickness of 5 nm, which corresponds to approximately 28 layers. This experimental value is consistent with the theoretical predictions. Their work also confirms the strong in-plane anisotropy of Se nanosheets through angle-resolved Raman spectroscopy.

T-Se has a similar structure to 1T-MoS_2, being seemingly formed by three layers[30]. *Ab initio* calculations performed using the Perdew–Burke–Ernzerhof (PBE)[35] functional yield a bandgap of 0.71, which decreases to 0.67 when considering spin-orbit coupling. Calculations with an HSE(+SOC) functional give a larger bandgap of 1.11 (1.04) eV[30]. T-Se does not exhibit anisotropy in its carrier mobilities, which were predicted to be 6.97 (9.48) 10^3 $cm^2V^{-1}s^{-1}$ for electrons (holes)[32]. These values are reasonably large when compared to various representative 2D materials[36]

1.3 Square selenene

The last predicted stable allotrope is square selenene (s-Se), which will be the focus of this thesis. We describe its spatial structure in Section 2.1. Square selenene was first predicted as a stable structure by Xian *et al.*[1] in 2017, as well as square tellurene. For the electronic properties, they predicted a highly

[2] All factors between carrier mobilities are calculated as $\frac{\max(\mu_x,\mu_y)}{\min(\mu_x,\mu_y)}$.

anisotropic semi-Dirac dispersion, which consists of a Dirac cone with linear dispersion in one direction and quadratic dispersion in the direction perpendicular to the first one, at a point along the ΓM_1 direction near the Fermi level. The complexity of this structure increases when considering that it is tilted in the ΓM_1 direction, which is highlighted by the different Fermi velocities: $0.68 \times 10^6 ms^{-1}$ from the "Dirac" point to Γ and $1.26 \times 10^6 ms^{-1}$ from the "Dirac" point to M_1 [30]. These values are comparable to the Fermi velocity in graphene, which is 10^6 ms^{-1}. When SOC is considered the cone-like structure opens near P_1, as shown later in Fig.4, forming a gap of 0.13 eV, which is practically unaltered when using HSE functionals[30].

Work done by Lin *et al.*[8] describes the calculation of the carrier mobility for T=300K. They found, in units of 10^3 $cm^2V^{-1}s^{-1}$, 93.2 (42.2) for electrons (holes) in the zigzag direction and 0.23 (0.69) for electrons (holes) in the armchair direction. This gives an anisotropy factor of approximately 405 (61) for electrons (holes), which is much larger than that for c-Se and t-Se, highlighting the highly anisotropic nature of s-Se. These predicted carrier mobilities are comparable to those of Ti_2CO_2(a typical MXene)[37], which also shares similar anisotropy factors of 121 (89) for electrons (holes), and are not that far from the carrier mobility of graphene, which is superior to 10^4 $cm^2V^{-1}s^{-1}$.

Square selenene has non-trivial topological properties, making it a topological insulator. Both Xian *et al.*[1] and Chen *et al.*[6] demonstrated this by calculating the Z_2 invariant through the evolution of Wannier charge centres. Furthermore, Chen *et al.*[6] also showed that square selenene has the potential to be used in novel tunable topological materials/devices due to the possibility of manipulating the topological phase (topological insulator $\leftrightarrow$ trivial insulator) via strain engineering.

1.4 Excitons

An exciton is a neutrally charged quasiparticle which consists of an electron and an electron hole, also known simply as a hole, bound together by the electrostatic Coulomb force due to their opposite charge. Quasiparticles, in condensed matter physics, are entities that simplify the treatment of the collective behaviour of multiple particles as if they were only one. The electron hole is itself a quasiparticle, formed when an electron transitions to a higher energy band from a full band, leaving behind an empty state. A good analogy, although quite crude, for the use of the electron hole to describe the collective behaviour of the electrons inside an almost full band is the "empty seat in an auditorium". Consider a long line of seats, each with a person seated except for one. We then ask each person to the left of the empty seat to move, one by one, to the right. Instead of looking at the movement of multiple people, we can analyse the movement of the empty seat, which seems to be moving to the left, hence the simplification

of the collective behaviour of a group as the movement of one entity. This way, the exciton simplifies the treatment of the interaction between one electron in the conduction band and the electrons in the almost full valence band.

Excitons can be divided into two categories depending on the spatial localisation of their wavefunction and their binding energy, those being Frenkel excitons and Wannier-Mott excitons. The first refers to excitons with restricted spatial distribution, concentrating around one or, at most, some unit cells. This type of exciton is more common inside insulators and organic semiconductors and tends to have smaller binding energies, around a few meV. The latter refers to excitons with a large spatial distribution, covering multiple unit cells. This category of excitons is much more prevalent in 2D materials. Due to their low dimensionality, the screening felt by the electron and the hole is weaker than if they were inside a 3D material; this, coupled with the geometrical confinement of the electrons in a plane, leads to a stronger interaction and consequently a more strongly bound exciton.

Due to their large binding energies, excitons in 2D materials can be stable at room temperature and will also dominate the optical response, thus justifying the study of their properties to determine the potential of materials in optics and optoelectronics[38].

Although the excitonic properties of Se atomic chains have already been studied[39], to the best of our knowledge, there have been no theoretical studies made on excitons in square selenene.

1.5 Thesis layout

This thesis is outlined as follows:

In Chapter 2, we study the electronic properties of square selenene using Density Functional Theory. We detail which software was used and its specificities. We then define the spatial structure of square selenene as well as the associated reciprocal space. Next, we perform the convergence of relevant parameters, while the rest of the chapter is dedicated to analysing the resulting band structure, for non- and fully relativistic calculations, spin texture in reciprocal space, as well as showing the existence of edge states in two different types of nanoribbons.

Chapter 3 is dedicated to the derivation of an effective Hamiltonian that describes the bandgap of square selenene when relativistic effects are considered. We first reproduce a $k{\cdot}p$ Hamiltonian from the literature and fit it to our DFT data. Then, we introduce various spin-orbit terms to describe the relativistic effects. Finally, we use this effective model to determine the effective masses of electrons and holes as well as the effective screening lengths for the two main directions (zigzag and armchair).

Finally, in Chapter 4, we find the ground-state exciton binding energy and wave function while considering the anisotropic nature of square selenene. Starting with the first-order interaction energy between a hole and an electron inside a 2D anisotropic semiconductor, which consists of the anisotropic case of the Rytova-Keldysh potential, we further approximate it to reduce computational effort. Finally, we find the energy functional associated with an anisotropic centre-of-mass Hamiltonian and the derived potential, using a trial wavefunction that takes into account anisotropy, and numerically minimise it to obtain the energy and wavefunction of the ground excitonic state.

As some final notes, all numeric and symbolic calculations, aside from DFT computations, were performed using *Python* (via *Jupyter* notebook[40] within the *Anaconda* distribution[41]) and the symbolic-calculation package *Mathematica*[42]. We also would like to note that the colour palette used throughout this thesis was chosen for its accessibility to colour blind people[43]. Finally, all figures are in *.pdf* format, so that they can be zoomed in without loss of quality (digital format only).

Chapter 2

Density Functional Theory

We commenced this thesis by studying the electronic properties of square selenene (s-Se) using Density Functional Theory (DFT). In particular, we used the open source software Quantum ESPRESSO (*QE*) [44] [45] to carry out the *ab initio* calculations. *QE* uses a plane-wave basis set together with pseudopotentials, which describe the interaction between valence electrons and the core, i.e., non-valence electrons and the nucleus. For our calculations, we used the Perdew-Burke-Ernzerhof (PBE) exchange-correlation functional [35], based on the Generalised Gradient Approximation (GGA). The PBE functional is considered by many as a staple, offering reasonable accuracy over a broad range of systems while being non-empirical. To emulate the core of selenium atoms, we used the norm-conserving, fully relativistic pseudopotential developed by A. Dal Corso (Quantum ESPRESSO distribution). The *k*-point mesh was generated using the Monkhorst-Pack method (MP) [46] with a shift. This shift is done to reduce the number of non-equivalent *k*-points, which aids the convergence of calculations. Although not the case in our work, for certain Bravais lattices (FCC, Hexagonal, and Orthorhombic F), this shift can be detrimental [47].

2.1 Crystal Structure

Square selenene consists of a square lattice with a basis composed of two selenium atoms. One of the atoms is located at the corner of the square unit cell, while the other is off-plane and slightly off-centred, being closer to the corner adjacent to the first atom in the *y*-direction. These two atoms correspond to two sublattices, labelled A and B. This spatial configuration leads to a buckled lattice, as shown in Fig. 1 (a), where we also show the 1st Brillouin zone. The initial structural parameters that we used were derived by Xian *et al.* [1] and are shown in Table. 1 .

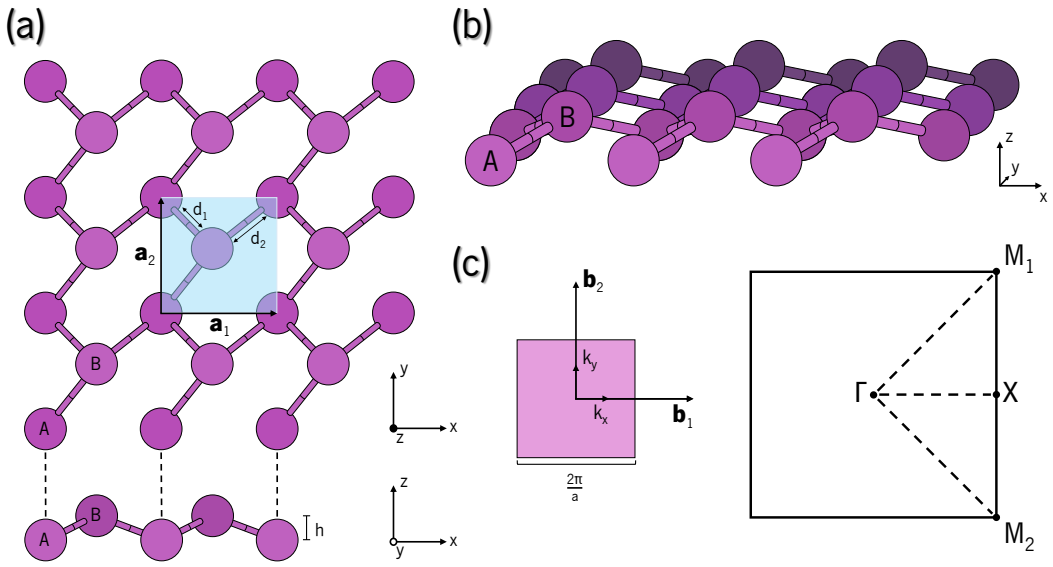


Figure 1: Spatial configuration of square selenene. (a) Top and side view. (b) Perspective view. (c) 1st Brillouin zone of s-Se with high symmetry points.

Table 1: Structural parameters of square selenene. We note that $|\mathbf{a}_1| = |\mathbf{a}_2| = a$. Data reproduced from the work of Xian *et al.*[1].

a(Å)	d_1(Å)	d_2(Å)	h (Å)
3.65	2.40	2.71	0.77

2.2 Convergence and structure optimisation

Before calculating properties of interest, we conducted convergence calculations to determine the optimal cut-off energy for the Kohn-Sham orbitals, *k*-point mesh size, and then performed lattice relaxation. The first two quantities are optimised by minimizing the total energy that comes from a self-consistent field (SCF) calculation while relaxation is performed using the "vc-relax" calculation of *QE*, where the lattice vectors and atomic positions are altered to meet the force threshold of 1×10^{-5}, in atomic units (a.u). The optimal parameters and their convergence are shown in Table.2 and Fig.2, respectively, and will be used in all DFT calculations unless otherwise indicated. From the relaxation, we obtained a lattice constant of 3.672 Å, which corresponds to an increase of approximately 0.6% compared to the work done by Xian *et al.*[1] and Liu *et al.*[30] and 0.05% when compared to the work done by Chen *et al.*[6]. We also tested the spatial configuration where the second Se atom sits above the centre of the unit cell. To do so, we performed relaxation runs where the atom was put in a position between the centre and the position we calculated. The atom always converged to its off-centre position unless it was put directly above the centre,

making it a metastable configuration.

Table 2: Converged parameters for DFT runs of the Kohn-Sham states energy cut-off and the size of the Monkhorst-Pack grid ($N \times N \times 1$).

Energy cut-off (Ry)	Monkhorst-Pack grid size
70	11

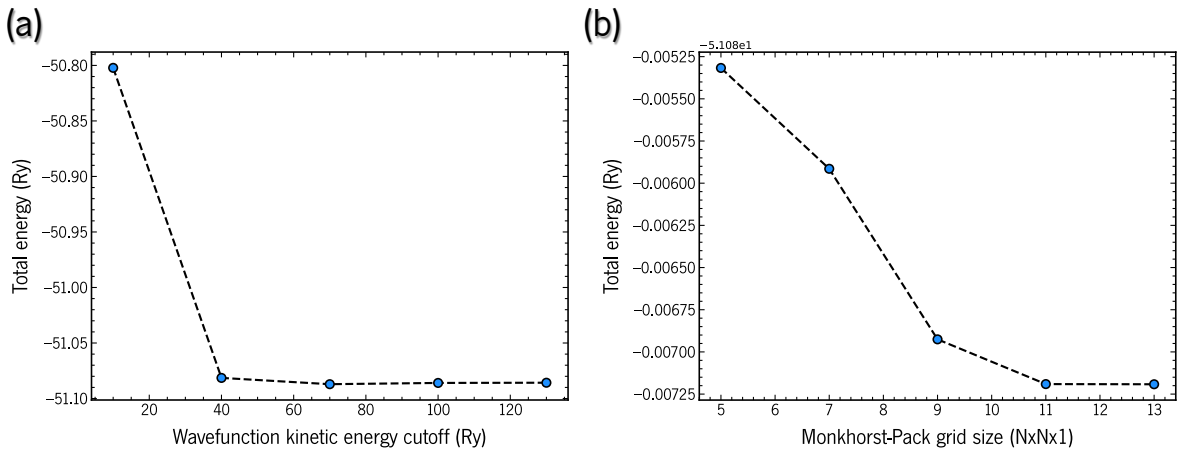


Figure 2: Total energy convergence with respect to: (a) Kohn-Sham states energy cut-off, (b) Monkhorst-Pack grid size ($N \times N \times 1$).

2.3 Band structure

In this section, we show the calculated band structure of square selenene, for non-relativistic (NR) and fully relativistic (FR) calculations[1] , along different k-(paths/areas) inside the 1st BZ.

Figure.3 shows the band structure along a path of high symmetry points - $\Gamma \rightarrow M_1 \rightarrow X \rightarrow M_2 \rightarrow \Gamma$. For the non-relativistic calculations, we have a Dirac-cone on the path between Γ and M_1, at a k-point we will denote as P_1=k_{P_1}(1,1) with k_{P_1}=0.20961 in crystal coordinates (c.c.), i.e units of $\frac{2\pi}{a}$. We note that at the corresponding point in the path ΓM_2, which will be denoted P_2, a similar structure seems to be emerging but falls short in forming a Dirac cone. This difference likely lies in the asymmetric nature of the spatial configuration of square selenene. The fully relativistic calculation opens a gap at P_1, with an additional splitting of about 10 meV, which further separates the bands into four (2 conductions bands $\rightarrow$ c_1, c_2 and 2 valence bands $\rightarrow$ v_1, v_2), as shown in Fig.4 . This fine split was not reported by previous

[1] For the fully relativistic calculations, we switched to fixed occupations to suppress numerical noise that could close the small bandgap.

works[1,6,30], which is likely due to the lack of fully relativistic calculations. As a precaution, we repeated the calculations with the lattice constants used in those works and found that the splitting still occurs.

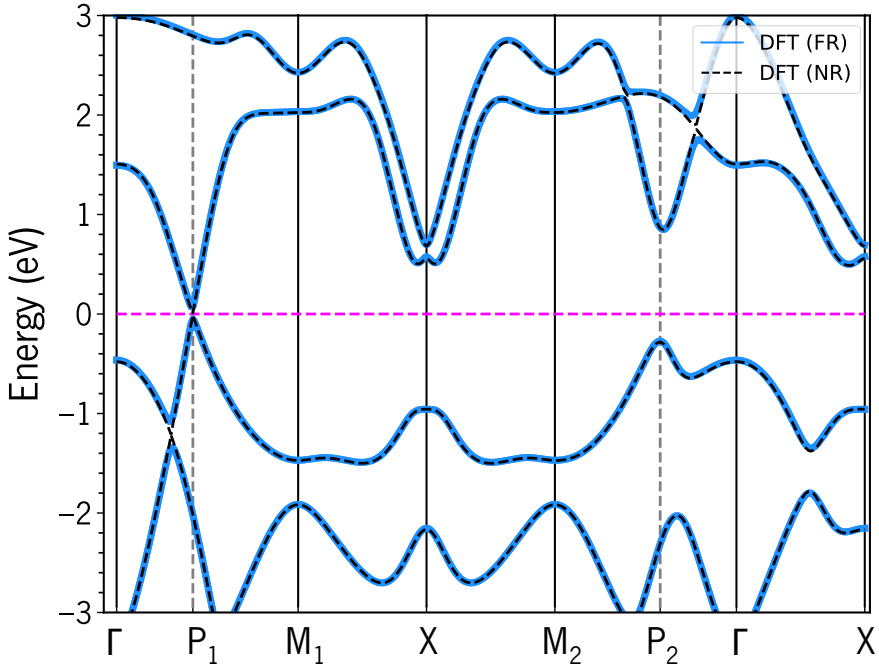


Figure 3: Band structure of square selenene obtained from DFT, for non- and fully relativistic calculations, on a path between high symmetry points in the 1st Brillouin zone. The energy reference is set as the energy of the Dirac cone-like structure at P_1.

Square selenene has an indirect bandgap of 0.101 eV and an optical transition at P_1 of 0.106 eV (c_1 - v_2), which indicates that s-Se is a narrow-gapped semiconductor, with a transition located in the mid infrared region of the electromagnetic spectrum. Our values for the bandgap are consistent with the literature[1,6,30]. While standard DFT calculations are known to underestimate bandgap energies, previous works using HSE functionals[1,30] have demonstrated that, for square selenene, the bandgap is practically unchanged.

Upon further inspection, we found that the Dirac-cone-like structure at P_1 is actually highly anisotropic, as shown in Fig.5(a), and also displays what is called semi-Dirac dispersion: linear dispersion along one direction and parabolic in the perpendicular direction. For square selenene, linear dispersion is present along the ΓM_1 direction, while parabolic behaviour is observed in the perpendicular direction at P_1. We represent these two main directions by considering the momentum displaced from P_1 - $\mathbf{q} = (q_{\parallel}, q_{\perp}) = \left(\frac{k_x+k_y}{\sqrt{2}} - \sqrt{2}k_{P_1}, \frac{k_y-k_y}{\sqrt{2}}\right)$ - and plot the cone along them in Fig.4. We note that this Dirac-like cone is slightly tilted in the $\parallel$ direction, as we will further explain in Chapter 3. For a better understanding of the band structure, we calculated it along the entire 1st Brillouin zone. The perspective render of the innermost

bands (highest/lowest valence/conduction bands) and the respective contour plots are represented in Fig.5. We immediately note that the band structure has reflection symmetry along the k_x=(-)k_y directions. This entails the existence of two gaps, the other one being located at P_1'.

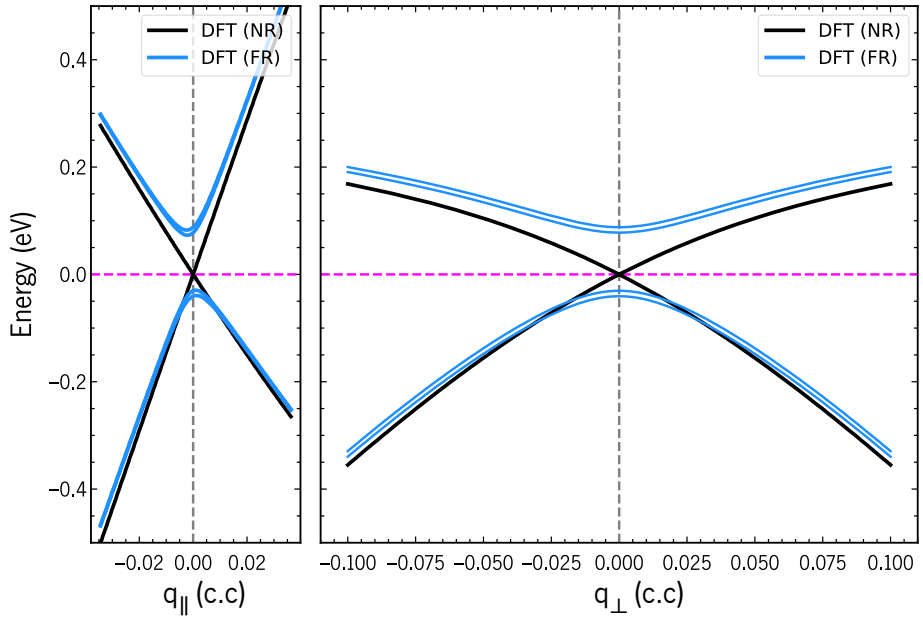


Figure 4: Band structure of square selenene obtained from DFT, for non- and fully relativistic calculations, around P_1 for the parallel ($q_{||}$) and perpendicular directions ($q_{\perp}$). Both graphs use the same scale to allow for direct comparison.

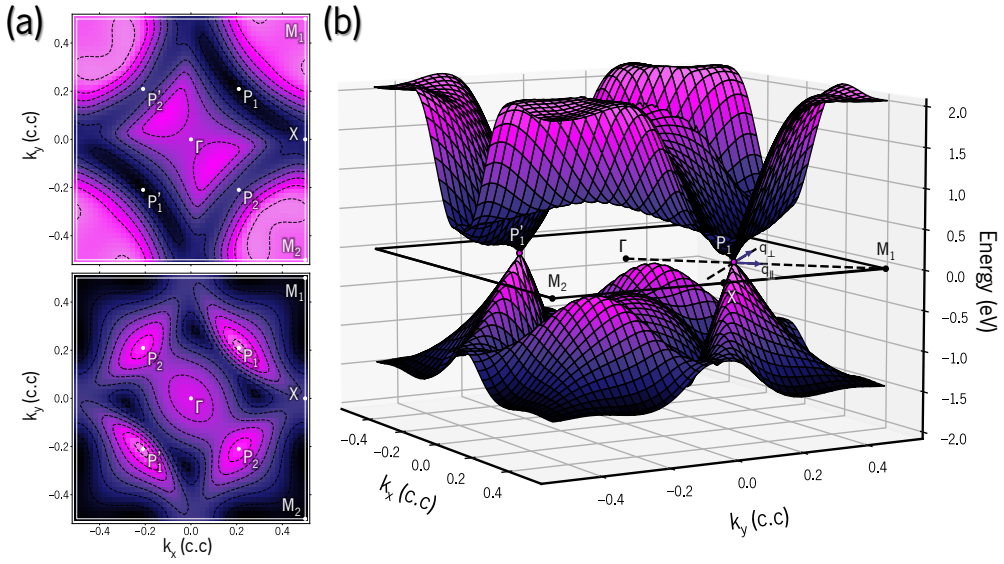


Figure 5: Valence and conduction band along the 1st Brillouin zone: (a) contour plots of the conduction (top) and valence (bottom) bands, (b) perspective render.

2.4 Spin texture

In this section, we present the expectation values of the spin components for each axis, i.e., $\langle S_x \rangle$, $\langle S_y \rangle$, and $\langle S_z \rangle$, associated with energy states across the entire Brillouin zone. These values were obtained using the Quantum ESPRESSO module **bands.x**, which calculates the expectation values of the spin operator on the spinor wavefunctions, which were computed using **pw.x**, along each band. When plotting the expectation values along the first Brillouin zone, we uncover an intricate spin texture, shown in Fig.6 and Fig.7. The most notable features are:

- A helical spin texture, called spin-momentum locking, around P_1 and P_1' that also acts like a spin-sink, i.e, as $\mathbf{k} \rightarrow P_1$ we have $\langle S_i \rangle \rightarrow 0$. This implies an increase of variance ΔS_i near the point, since $\langle S^2 \rangle = \sum_i \langle S_i \rangle^2 + (\Delta S_i)^2$. We note that this spin pattern also has a clear separation of S_z components (positive and negative), divided along the $q_\perp$ direction.

- In the k_y = -k_x line, for the valence bands, we can see what looks like a source and sink of spin (located near P_2 and P_2'). The source and sink are permuted when switching between valence bands.

- The spin texture around Γ seems to be mainly aligned with the k_y = -k_x direction, with the orientation depending on the band.

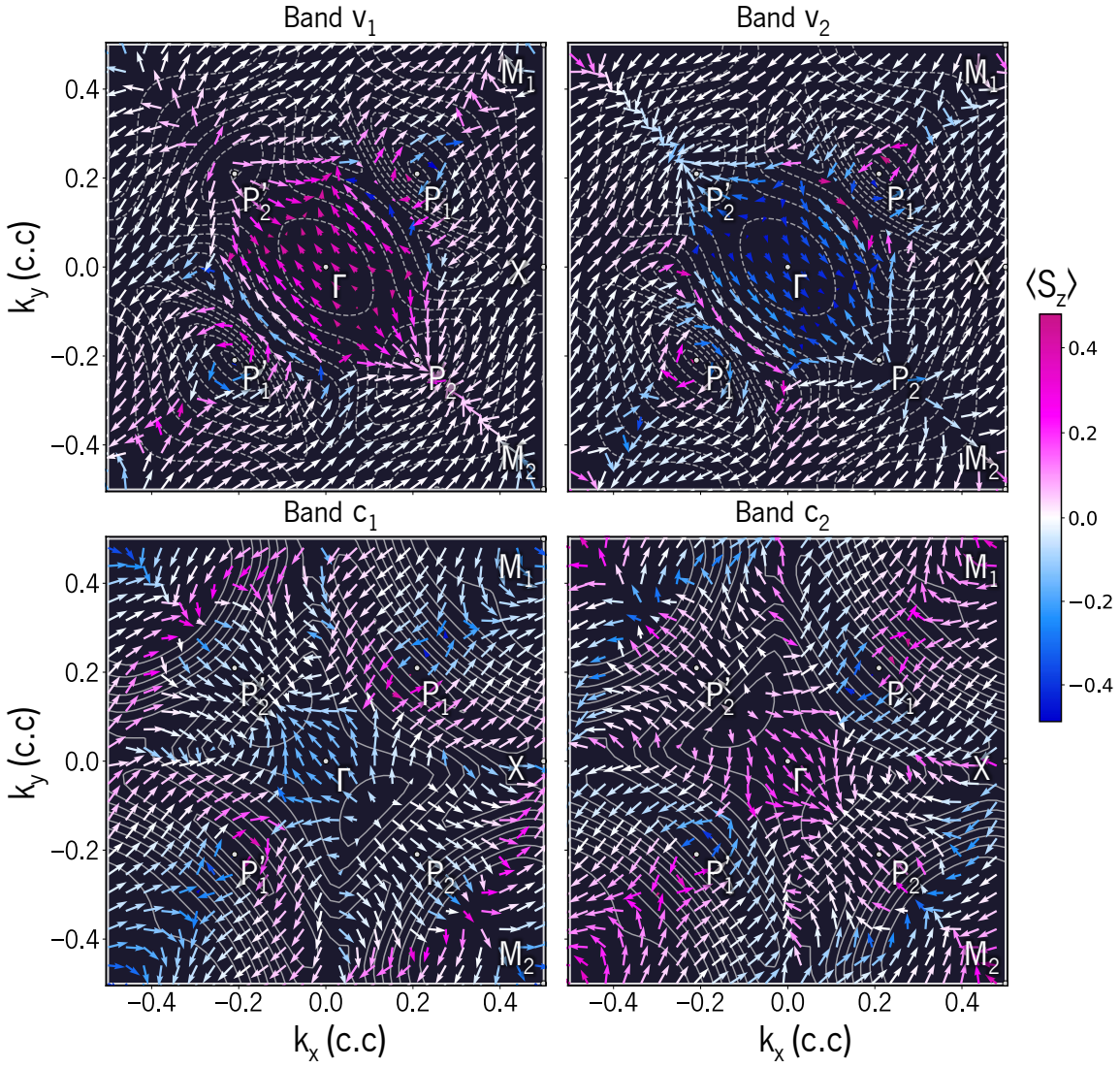


Figure 6: Spin texture of square selenene, constructed through the expected values of the spin operators - $\langle S_i \rangle$ - obtained from DFT along the entire 1st BZ. The arrows represent the *x* and *y* components, while the *z* component is represented using a colour scale.

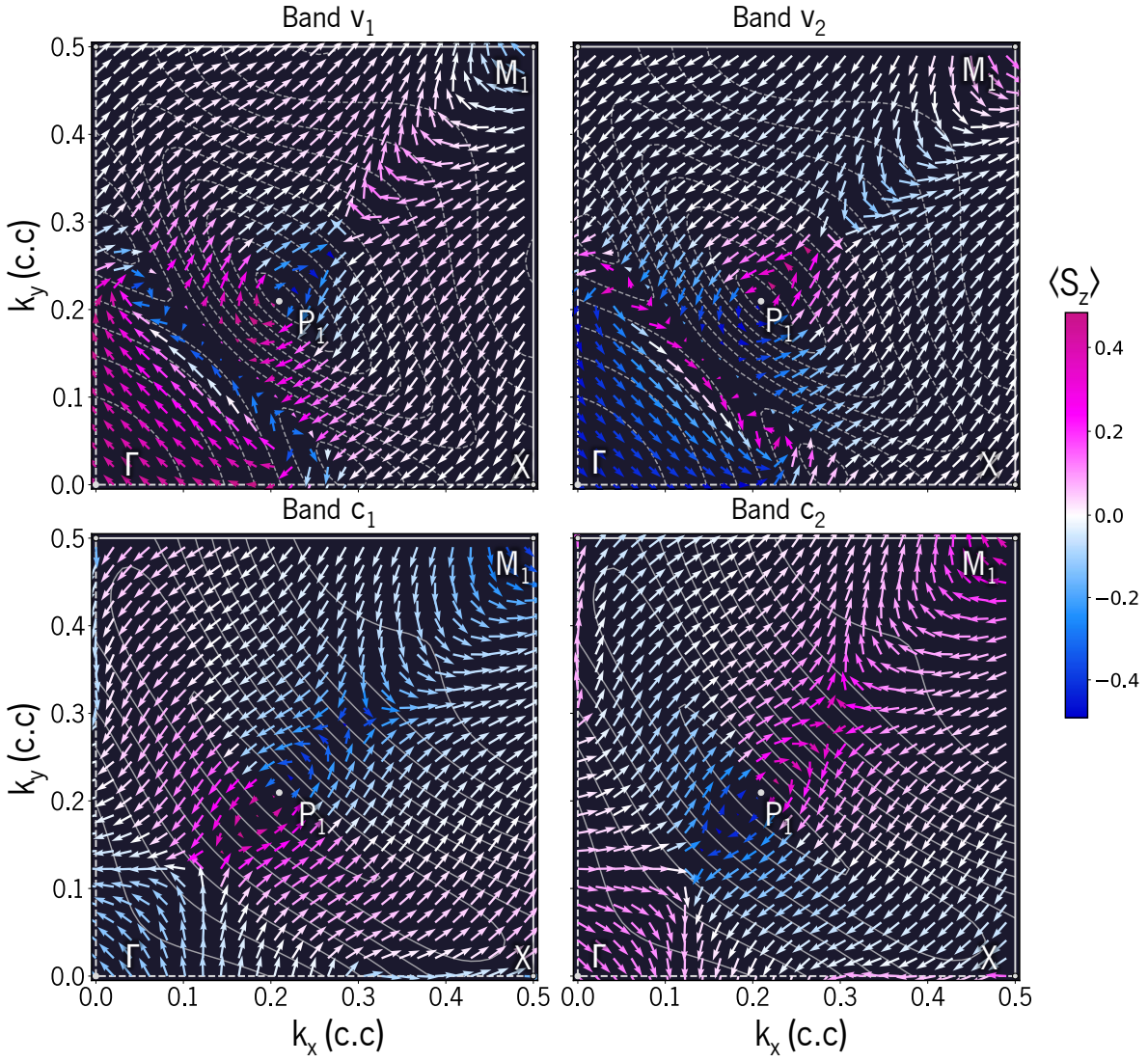


Figure 7: Spin texture of square selenene, constructed through the expected values of the spin operators - $\langle S_i \rangle$ - obtained from DFT along the first quadrant of the 1st BZ. The arrows represent the *x* and *y* components, while the *z* component is represented using a colour scale.

2.5 Edge states

To probe the existence of edge states in square selenene, we modelled nanoribbons using two types of cuts inspired by graphene: zigzag and armchair. To easily build these two types of nanoribbons, we rotated and scaled the square unit cell so that its side became the length of the original unit cell's diagonal, as shown in Fig.8 . The size of the new unit cell vectors is given by the old ones times $\sqrt{2}$. The new unit cell contains 4 atoms.

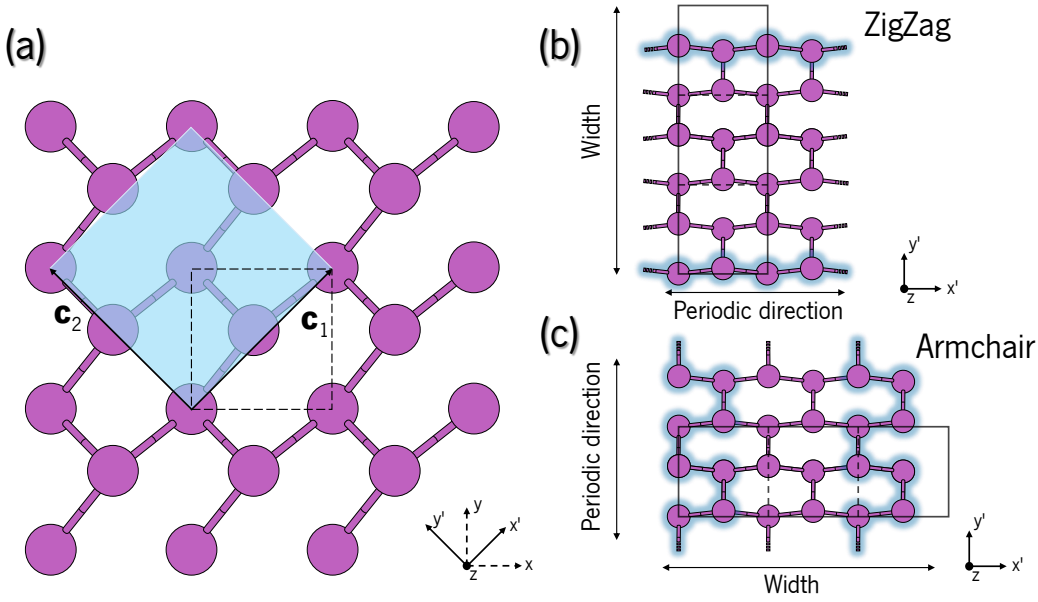


Figure 8: (a) Rotated and scaled cell of square selenene. s-Se nanoribbon with a supercell, built from 3 new cells, to form : (b) a zigzag cut and (c) an armchair cut. The name of the cuts alludes to the shape of the nanoribbon's edge along the periodic direction, which is highlighted in blue.

We considered nanoribbons with a supercell built from 20 of these new unit cells, which gives a width of approximately 10 nm. The edges were passivated with hydrogen atoms [2], which were relaxed along the width, to eliminate edge states associated with dangling bonds. We then obtained the band structure from Γ to X, shown in Fig.9(a) and Fig.10(a), using a cut-off energy of 90 Ry and $13 \times 1 \times 1$ ($1 \times 13 \times 1$) MP grid size for the zigzag (armchair) cut.

To search for edge states, we employed the post-processing code **pp.x** from *QE*. This allowed us to obtain the contribution of states, specified by the band number n and k-point k, to the charge density - $\rho_k^n(x, y, z)$. To illustrate the localization of this states along the x and y axes, we collapsed the z-direction by summing over it, i.e., $\varrho_k^n(x, y) = \sum_z \rho_k^n(x, y, z)$, and show the result in Fig.9(b) and Fig.10(b).

[2] Two and four hydrogen atoms per unit cell for the zigzag and armchair, respectively.

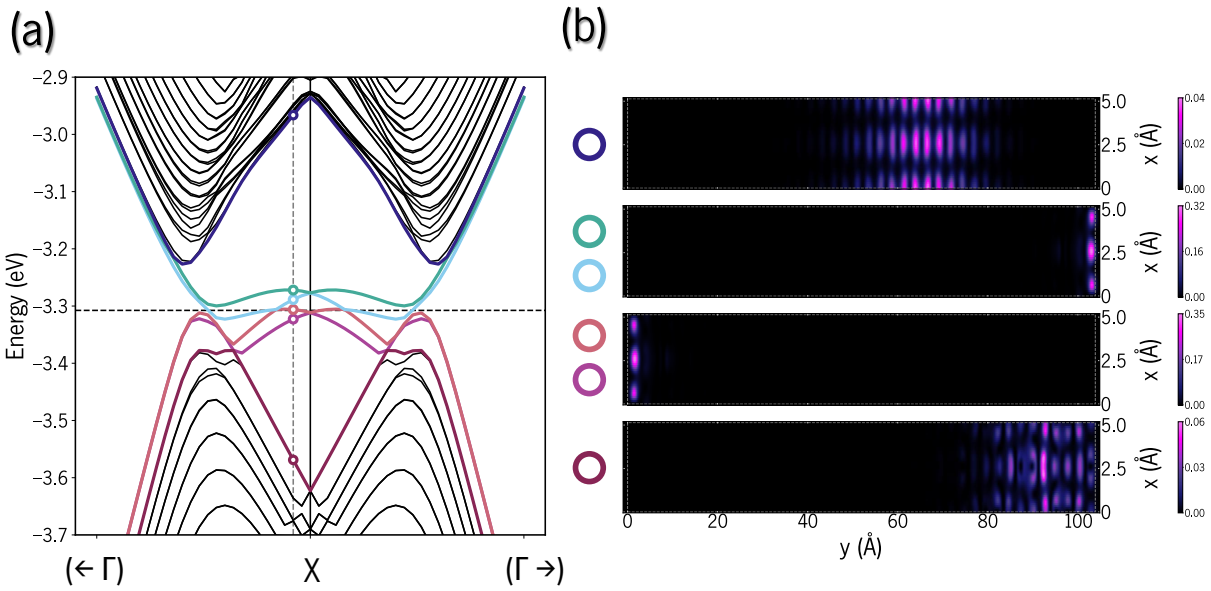


Figure 9: (a) Electronic band structure of a square selenene zigzag nanoribbon with a width of ≈10 nm. (b) Collapsed contribution to the charge density of the states located at the vertical grey dashed line, for different bands. The colour bar is in units of e/a_0^3, while the bands and the collapsed contribution to the charge density are colour coded to indicate correspondence.

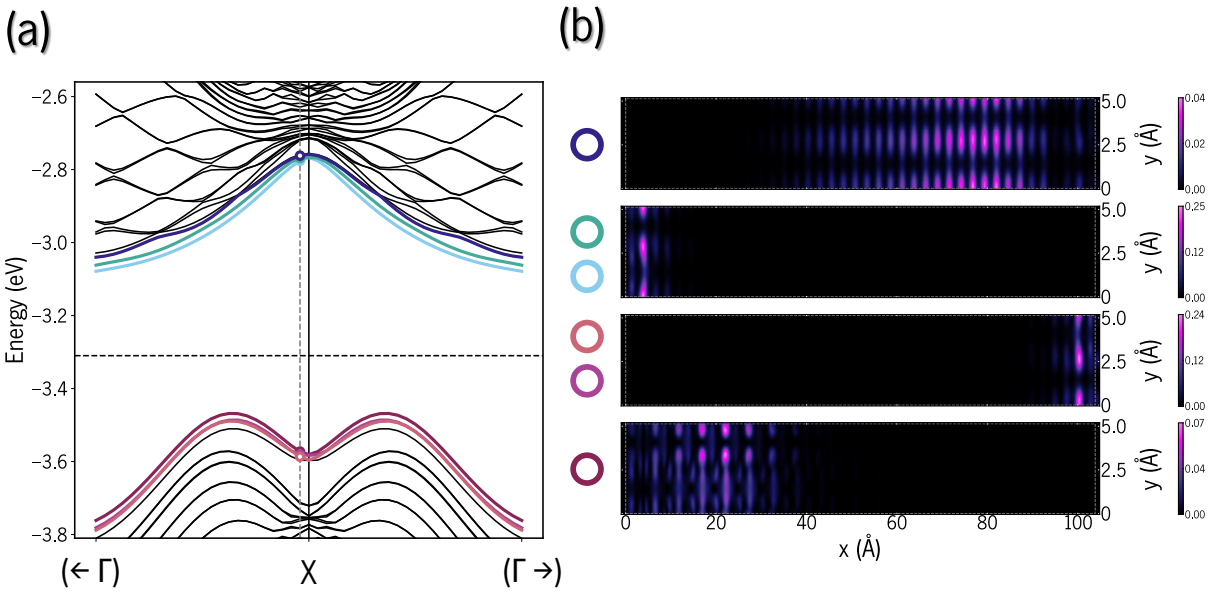


Figure 10: (a) Electronic band structure of a square selenene armchair nanoribbon with a width of ≈10 nm. (b) Collapsed contribution to the charge density of the states located at the vertical grey dashed line, for different bands. The colour bar is in units of e/a_0^3, while the bands and the collapsed contribution to the charge density are colour coded to indicate correspondence.

We obtain edge-states in both cases; however, only the zigzag cut presents states that cross the gap, which is a characteristic of topological states. The non-trivial topological nature of square selenene was confirmed by Xian *et al.*[1] and Chen *et al.*[6] using the evolution of Wannier charge centres in zigzag cut nanoribbons to calculate the topological invariant Z_2. We note that in our case, we have 4 states that cross the gap, while the cited works only show 2. This is due to the further splitting we obtained.

Chapter 3

Effective Model

In this chapter, we construct a 4-band effective Hamiltonian and fit it to the data obtained from fully relativistic DFT computations. The base is the $k{\cdot}p$ Hamiltonian presented by Xian *et al.*[1], that accurately describes the dispersion around P_1 when SOC effects are not considered. We then add various SOC terms until the fit is satisfactory. Finally, we add an extra term to replicate the spin texture around P_1 qualitatively.

3.1 k·p Hamiltonian

The cornerstone of our effective model is the semi-Dirac effective Hamiltonian, obtained through $k{\cdot}p$ perturbation theory[48], with the form

$$H_{k\cdot p} = \epsilon(\mathbf{q})\,(\sigma_0 \otimes s_0) + [\mathbf{h}(\mathbf{q}) \cdot \boldsymbol{\sigma}] \otimes s_0 \tag{3.1}$$

where $\boldsymbol{\sigma} = (\sigma_x, \sigma_y, \sigma_z)$ is a vector whose components are the Pauli matrices associated with the sublattice degree of freedom, s_0 is the identity matrix (dim=2) associated with the spin degree of freedom and

$$\epsilon(\mathbf{q}) = -Aq_{\parallel} - Bq_{\perp}^2, \tag{3.2}$$

$$\mathbf{h}(\mathbf{q}) = (Cq_{\parallel} + Dq_{\perp}^2, Fq_{\perp} + Gq_{\parallel}q_{\perp}, 0). \tag{3.3}$$

This implies that we are working in the basis $\{|A,\uparrow\rangle; |A,\downarrow\rangle; |B,\uparrow\rangle; |B,\downarrow\rangle\}$, where A and B represent the two sublattices, labelled in Fig.1. The diagonalisation of this Hamiltonian leads to two different eigenvalues (equivalent to dispersion curves), each with multiplicity 2, given by

$$E_{\pm}(q_{\parallel}, q_{\perp}) = -Aq_{\parallel} \pm Bq_{\perp}^2 \pm \sqrt{\left(Cq_{\parallel} + Dq_{\perp}^2\right)^2 + \left(Fq_{\perp} + Gq_{\parallel}q_{\perp}\right)^2}. \tag{3.4}$$

These curves highlight the tilted nature of the semi-Dirac cone. If we only consider the parallel direction, Eq.(3.4) becomes:

$$E_{\pm}(q_{\parallel}, 0) = -Aq_{\parallel} - |Cq_{\parallel}|, \tag{3.5}$$

which implies that the cone is formed by two different slopes: $-A + |C|$ when $q_{\parallel} < 0$ and $-A - |C|$ when $q_{\parallel} > 0$.

We fitted Eq.(3.4) to our DFT data, considering k-points along the 1st Brillouin zone[1] with energy lying in the [-0.2,0.2] eV range. We used the non-linear least-squares method, with a weight following a three-parameter Lorentzian function (I =1, E_0=0 eV, γ=0.1 eV) to prioritise points with energy closer to zero. The fitted parameters are displayed in Table.3 . The parameters marked with an asterisk (*) have an ambiguous sign. Altering the sign of any of them, one at a time, will not alter the fit result in the main directions and only slightly alter the quality of the fit in the other regions. However, the sign change has an impact on other quantities than the band structure, as we will show later when examining the spin texture of the effective model. The fit follows very closely the DFT curves in the main directions, and displays small deviations outside of them, as shown in Fig.11 .

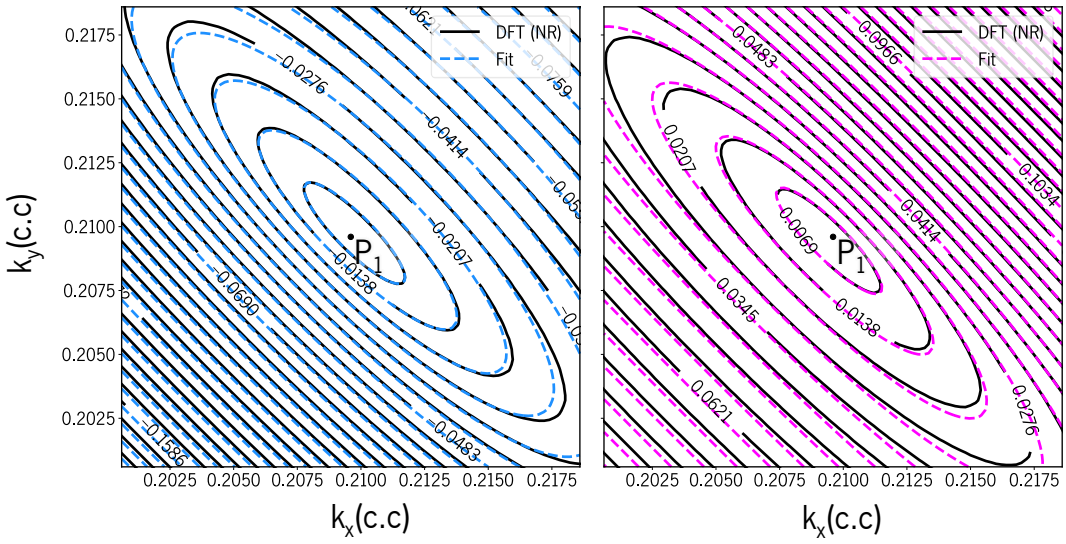


Figure 11: Contour plots of the valence (left) and conduction (right) bands that form the semi-Dirac cone near P_1, obtained from NR DFT calculations (solid black lines) and compared to the fitted $k{\cdot}p$ model (dashed coloured lines).

[1] It is important to consider points outside the main directions since there are terms $\propto q_{\parallel} q_{\perp}$.

Table 3: Fitted parameters of the k·p Hamiltonian.

A (eV·Å)	B (eV·Å^2)	C^* (eV·Å)	D^* (eV·Å^2)	F^* (eV·Å)	G^* (eV·Å^2)
-1.964	6.179	6.417	-9.836	1.513	-26.67

3.2 Spin-orbit model

To obtain an accurate effective model of the fully relativistic DFT data, we introduced two terms to describe SOC effects. To do so, we considered the Hilbert space associated with the spin degree of freedom, which is represented by the matrices s_i that follow the structure of Pauli matrices. We first considered intrinsic spin-orbit coupling, for which the Hamiltonian is given by

$$H_{\mathrm{SO}}(\Delta_{\mathrm{SO}}) = \Delta_{\mathrm{SO}}(\sigma_z \otimes s_z), \tag{3.6}$$

where Δ_{SO} is the magnitude of the spin-orbit interaction energy. This term is responsible for the opening of the main gap, as seen in Fig.13 .

We then considered Rashba spin-orbit coupling due to the lack of inversion symmetry in square selenene[49]. However, if included in our effective model, it cannot produce 4 distinct eigenvalues at **q**=**0**. We introduced anisotropy by splitting the Rashba constant – α_{R} – into two –$\alpha_{\mathrm{R}}^{xy}, \alpha_{\mathrm{R}}^{yx}$–, which allows 4 distinct eigenvalues at P_1, as shown in appendix B. This term is considered to replicate the further splitting of the bands near P_1, as shown in Fig.13, and has the form

$$H_{\mathrm{R}}^{\mathrm{ani}}(\alpha_{\mathrm{R}}^{xy}, \alpha_{\mathrm{R}}^{yx}) = \alpha_{\mathrm{R}}^{xy}(\sigma_x \otimes s_y) - \alpha_{\mathrm{R}}^{yx}(\sigma_y \otimes s_x), \tag{3.7}$$

which was also used by Geldiyev *et al.*[50] to describe a flat square lattice of Te atoms on a Au(100) surface.

Finally, to replicate qualitatively the expected values $\langle S_z \rangle$ obtained from DFT, we introduce the term given by

$$H_{\mathrm{Sz}}(q_{\parallel}, M_z) = M_z q_{\parallel} \left(\sigma_0 \otimes s_z\right), \tag{3.8}$$

which is not necessary for a good fit of the bands but is needed to obtain a qualitatively similar spin texture near P_1.

The final effective model is given by

$$H_{\mathrm{eff}} = H_{k\cdot p}(\mathbf{q}, A, B, C, D, F, G) + H_{\mathrm{SO}}(\Delta_{\mathrm{SO}}) + H_{\mathrm{R}}^{\mathrm{ani}}(\alpha_{\mathrm{R}}^{xy}, \alpha_{\mathrm{R}}^{yx}) + H_{\mathrm{Sz}}(q_{\parallel}, M_z), \tag{3.9}$$

while the minimum effective model only removes H_{Sz}. We fitted Eq.(3.9), with and without H_{Sz}, to DFT data along $q_{\parallel}$ and $q_{\perp}$ within the energy range [-0.1,0.1] eV, using the non-linear least-squares method and obtained the parameters shown in Table 4. We present the DFT data and the resulting fit in Fig.12, and compare the spin texture around P_1 obtained from FR DFT calculations (Fig.14) with that derived from our effective model (Fig.15). The effective model offers an accurate description of the bandgap, with small discrepancies in the perpendicular direction. This implies the presence of Rashba SOC effects in square selenene, which is common in systems that lack symmetry of inversion[49]. Upon further inspection, the spin-momentum locking around P_1 is reminiscent of the spin texture due to Rashba effects[51,52]. However, the usual band structure, with a double degeneracy of the bands at a point, is not present in square selenene. As discussed by Lee *et al.*[53], the conventional Rashba bands are doubly degenerate at time-reversal invariant momenta (TRIM) in non-centrosymmetric materials. We believe that conventional Rashba effects are present in square selenene and that the degeneracy is not enforced since P_1 is not a TRIM[2].

We also qualitatively reproduced the spin texture around P_1 of the valence bands, namely the chiral pattern that behaves like a sink for the expected values of the spin operators. We note that the sign of M_z, which is not determined by the fit routine, decides which side of the spin pattern has a positive/negative expected value of the S_z operator. The spin texture of the conduction bands that come from our effective model does not match the pattern from DFT, since we got a saddle-like configuration. This indicates that other types of SOC might be present, whose effects are more noticeable in the spin-texture.

An accurate representation of the spin texture would probably require a different model as well as a more complex fitting routine, in the sense that the bands and the mean values of the spin operators would need to be fitted simultaneously. We also note that the chirality of the spin texture near P_1 depends on the combined signs of the fit parameters C and F of the $k{\cdot}p$ hamiltonian: the chirality changes when both parameters are negated. We note that changing the sign of C and F worsens the fit, except along the main directions, which further emphasises the need for a better model if the goal is to reproduce the spin texture.

Table 4: Fitted parameters of the effective model, with and without H_{Sz}.

$\lvert M_z\rvert$ (eV · Å)	Δ_{SO}(eV)	α_R^{xy}(eV)	α_R^{yx}(eV)
6.5542×10^{-2}	5.7584×10^{-2}	1.8803×10^{-4}	6.8225×10^{-3}
-	5.7588×10^{-2}	1.8321×10^{-4}	6.8658×10^{-3}

[2] For a square Brillouin zone, the TRIM are Γ, X, Y, and M.

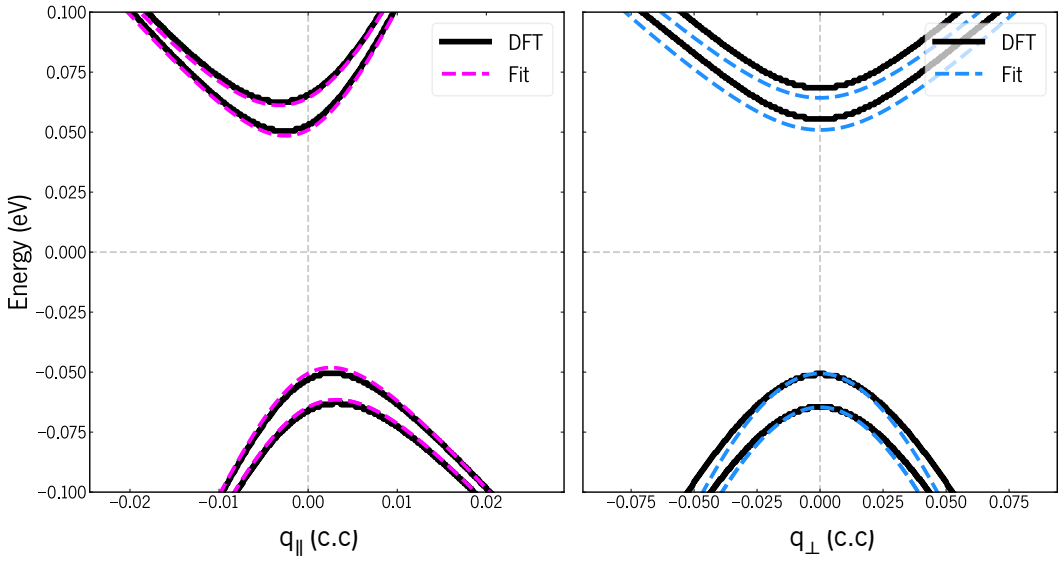


Figure 12: Bandgap along the main directions obtained from FR DFT calculations (black lines) compared to the fitted effective model (coloured dashed lines).

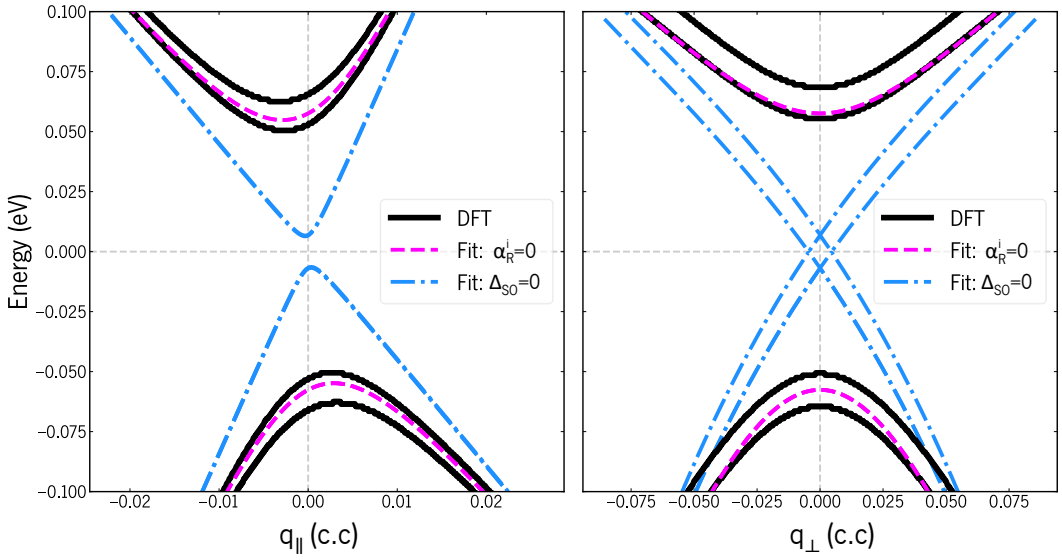


Figure 13: Bandgap along the main directions obtained from FR DFT calculations (black lines) compared to the fitted effective model, when Δ_{SO}=0 (dash-dotted blue lines) and $\alpha_R^{xy} = \alpha_R^{yx} = 0$ (dashed fuchsia lines).

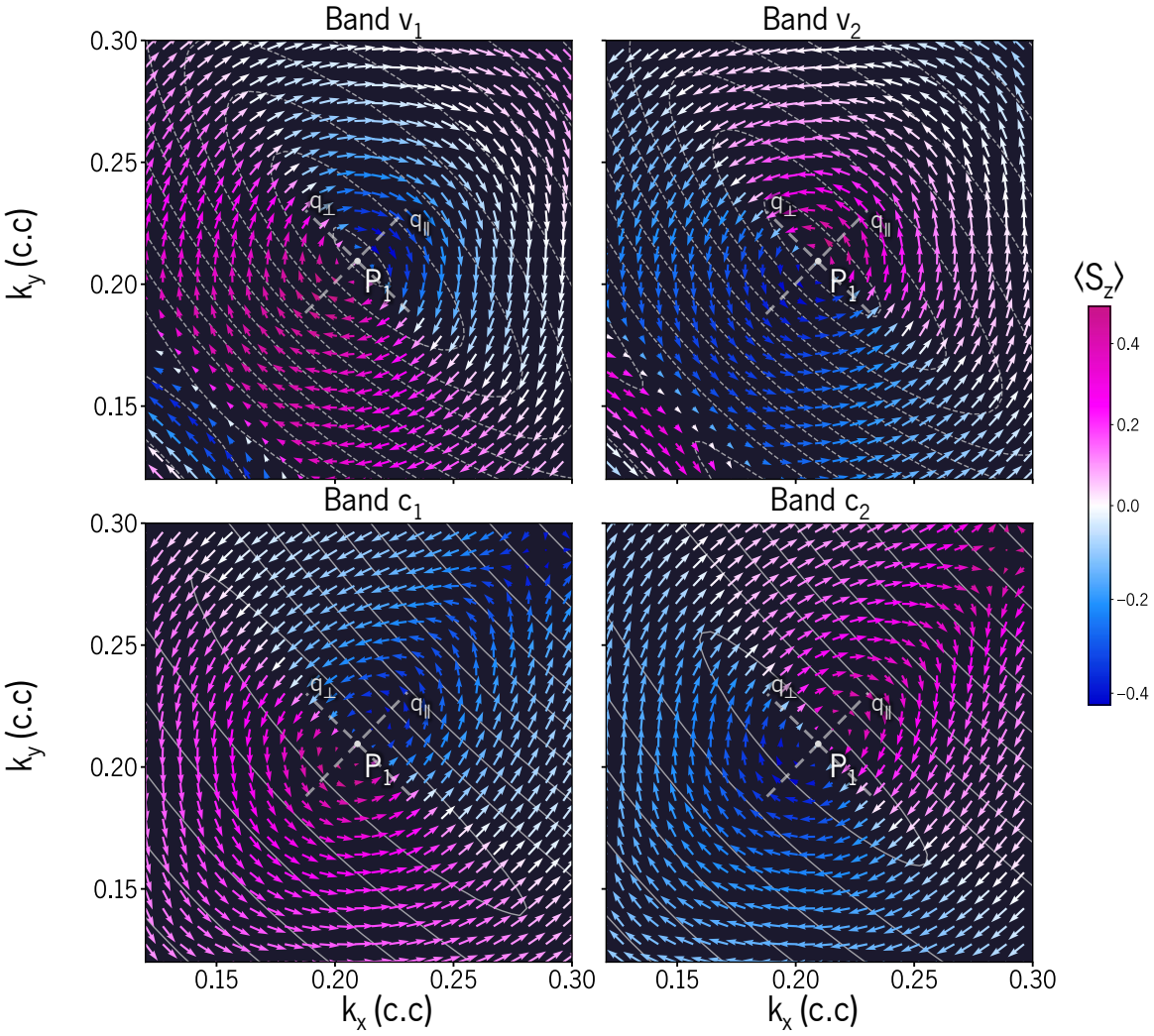


Figure 14: Spin texture of the bands near P_1 obtained from FR DFT calculations. The arrows represent the x- and y-components of $\langle S_i \rangle$, while the colours represent the z-component.

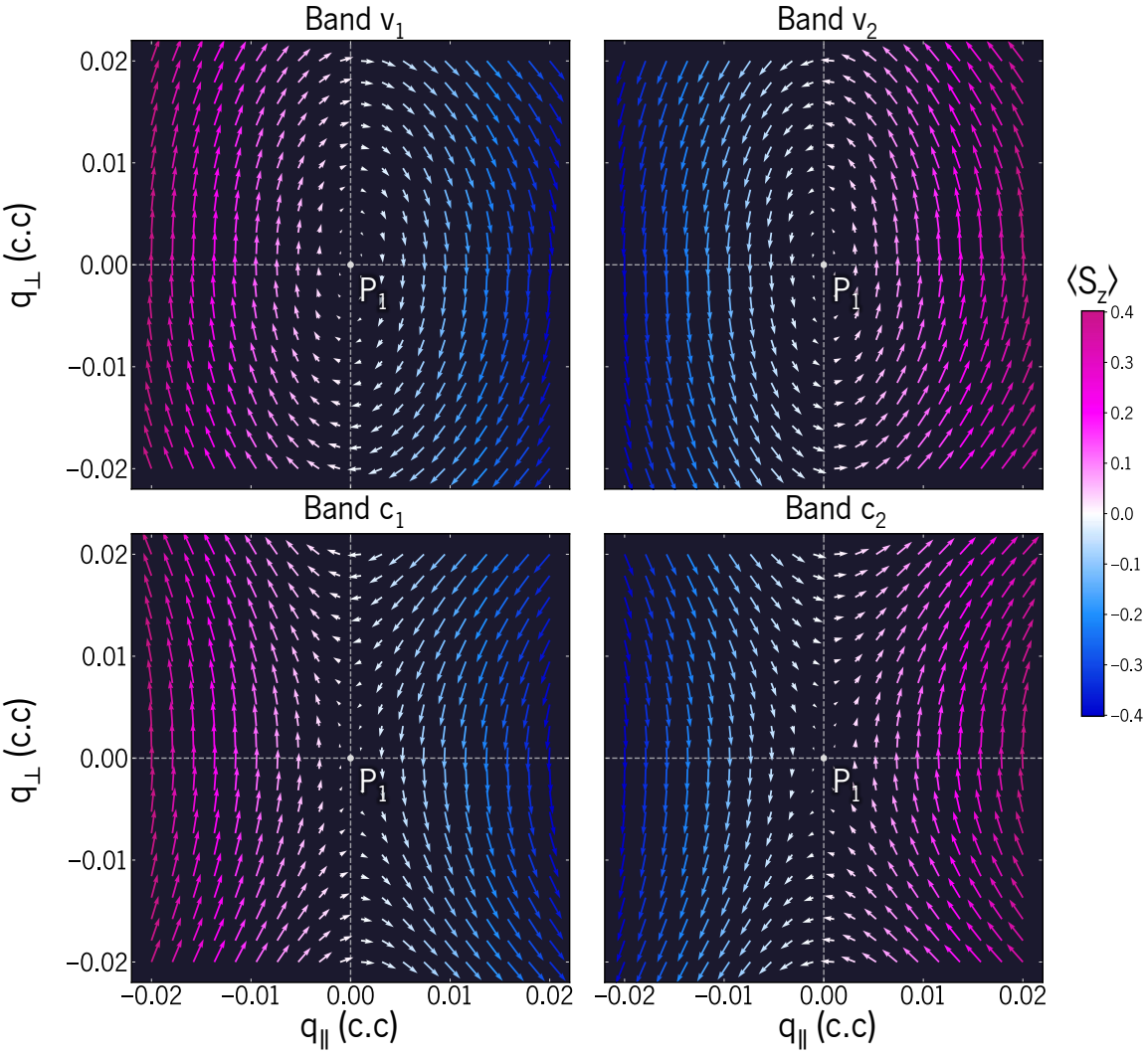


Figure 15: Spin texture of the bands near P_1 obtained from our effective model (with H_{S_z}). The arrows represent the *x*- and *y*- components of $\langle S_i \rangle$, while the colours represent the *z*-component.

3.3 Effective Masses

In this part, we extract the effective masses for holes and electrons along the ||- and ⊥- direction from our effective model and from a real-space Hamiltonian generated by the software PAOFLOW[54](see Appendix A), using the definition

$$m_i^n = \hbar^2 \left(\frac{\partial^2 E_i^n(\mathbf{q})}{\partial \mathbf{q}_i^2} \right)^{-1}, \tag{3.10}$$

where n and i are the index for the bands and main directions (|| or ⊥) respectively. The values we calculated can be found in Table.5, alongside the values from Lin *et al.*[8].

Table 5: Effective masses for holes and electrons along the along the ||- and ⊥- direction, in terms of the electron mass m_0, derived from the effective model and the Hamiltonian from PAOFLOW. The last row contains the data reproduced from the work of Lin *et al.*[8].

	$m_{\parallel}^e$	$m_{\parallel}^h$	$m_{\perp}^e$	$m_{\perp}^h$
PAOFLOW	0.0108	0.0119	0.2464	0.1653
Effective model	0.0109	0.0109	0.2794	0.1458
Lin *et al.*[8]	0.044	0.039	0.52	0.35

As expected from the dispersion, the effective masses are quite different depending on the main direction, being ∼10 smaller along the ||-direction. The hole and electrons have the same effective mass in the ||-direction, while the electron effective mass is approximately two times larger than the hole effective mass when considering the ⊥-direction. The results between PAOFLOW and the effective model are quite close while being consistent with the effective masses obtained by Lin *et al.*[8]. As expected, the effective mass of holes in the ⊥-direction is smaller when extracted from our effective model, since the valence band curvature is larger than the one in the DFT data, which is perfectly replicated by the PAOFLOW Hamiltonian (see Fig.23). Lin *et al.*[20] also obtained effective masses around $10^{-2} m_0$ in the parallel direction and $10^{-1} m_0$ for the perpendicular direction, as well as a bigger effective mass for electrons. Beyond the numerical value differences (a missing factor of ≈4 for the ||-direction and ≈2 for the ⊥-direction), they found the effective masses in the parallel direction to be different from each other. The values for the effective masses in the ⊥-direction are well within the norm of 2D semiconductors, while being relatively small in the ||-direction[55].

3.4 Effective Screening Lengths

In 3D crystals, macroscopic screening can be characterised by a dielectric constant specific to each material. However, for 2D crystals, this description is no longer valid due to *q*-dependence of the dielectric function[3], calling for a new way to describe screening effects[56]. Screening in two-dimensional materials is dictated by the 2D layer polarizability, given by[57]

$$\alpha^{2D} = \frac{r_0}{2\pi}, \tag{3.11}$$

where r_0 is the screening length. This polarizability can be derived using *ab initio* methods, considering a stack of layers separated by a distance *L*. By calculating the in-plane dielectric constant for increasingly larger values of *L*, one can extract α_{2D}, as explained by Cudazzo *et al.*[56] and executed by Berkelbach *et al.*[58]. For the anisotropic case, one must apply the method to the dielectric tensor and look at the convergence of the *xx* and *yy* components. For simplicity, we chose an alternative to calculate the effective screening lengths, which uses our effective model and the following formula[59], also derived by Jian *et al.*[60]

$$r_{0i} = 4\pi\hbar c\alpha \sum_{\tau}\sum_{c,v}\int \frac{d^2\mathbf{q}}{(2\pi)^2} \frac{\left|\left\langle u^c_{\mathbf{q}}\right| \frac{\partial}{\partial q_i} H_{eff}(\mathbf{q}) \left|u^v_{\mathbf{q}}\right\rangle\right|^2}{\left[E_c(\mathbf{q}) - E_v(\mathbf{q})\right]^3}, \tag{3.12}$$

where τ indexes the valleys, *c* and *v* the conduction and valence bands, $\left|u^n_{\mathbf{q}}\right\rangle$ is the spinor at $\mathbf{q}$ for the n^{th} band and $E_n(\mathbf{q})$ the energy at $\mathbf{q}$ of the n^{th} band. We note that typical DFT methods consider several band transitions, whereas the use of Eq.(3.12) on our effective model only considers four bands, yielding an estimation of the screening lengths. One could also consider larger gapped structures for a more accurate value, as done by Jian *et al.*[60]; however, the main contributions for square selenene come from the narrow gap ($E_g \approx 0.1$ eV). For comparison, the structure at P_2 has a gap of $\sim$1 eV.

A more detailed *ab initio* study of square selenene would be needed for more accurate values of the screening lengths, which is beyond the scope of this thesis. Applying Eq.(3.12) to our effective model returns the values given in Table.(6), which can be considered estimations for the lower bounds of the screening lengths in square selenene.

Once again, the anisotropic nature of square selenene is highlighted here, with a factor of $\approx$3 between the two screening lengths. For comparison, this factor for phosphorene is approximately 1.057 ($\alpha^{2D}_{xx} = 4.20$Å, $\alpha^{2D}_{yy} = 3.97$Å)[61]. Another point worth noting is that the values are quite large, especially in

[3] In this case, q refers to a reciprocal space variable originating from a Fourier Transform.

Table 6: Effective screening lengths of square selenene along the ||- and ⊥- direction obtained from our effective model.

$r_{0\|\|}$(Å)	$r_{0\perp}$(Å)
1691 .08	455.25

the ||-direction. A similar gapped material, stanene ($E_g \approx 0.1$ eV), has a screening length of 351.85 Å[60], which is consistent with the value in the ⊥-direction but much smaller when compared with the value we obtained along the ||-direction. These large values are partially due to the small gap and the contribution of both valleys, which leads to an additional factor of 2. However, especially due to the large value along the ||-direction, a more detailed *ab initio* study should be conducted.

At first glance, it might seem strange that the screening length in the ||-direction is larger, since the dispersion curves are flatter in the ⊥-direction, as illustrated in Fig.4. This seems to imply that the denominator in Eq.(3.12) should be smaller for the same $|q_i|$ values. One difference might lie in the mean value of the derivative of the Hamiltonian; however, there is another distinction - the semi-Dirac dispersion of the cone. The dispersion curves in the ⊥-direction are quadratic, so the denominator in Eq.(3.12) will diverge to ∞ faster than in the ||-direction, leading to a smaller value of the screening length.

A possible next step, without using more advanced methods, would be to apply Eq.(3.12) to the Hamiltonian obtained from PAOFLOW. It would allow for more accurate values of the screening lengths, since one could consider more band transitions, as well as integrate over the entire 1st Brillouin zone. This set of values could be compared with the ones obtained from the effective model and, eventually, from *ab initio* calculations.

Chapter 4

Excitons

In this chapter, we use the variational method to calculate the ground state energy and wavefunction of excitons in square selenene (see Fig.16 for a stylised illustration). The effective Hamiltonian, which will be used to describe excitons in square selenene, is given by

$$\begin{aligned} H_{\bigcirc} &= \frac{P_{\parallel}^2}{2\mu_{\parallel}} + \frac{P_{\perp}^2}{2\mu_{\perp}} + \mathrm{V}_{\bigcirc}(r,\theta) \\ &= -\frac{\hbar^2}{2\mu_{\parallel}}\frac{\partial^2}{\partial r_{\parallel}^2} - \frac{\hbar^2}{2\mu_{\perp}}\frac{\partial^2}{\partial r_{\perp}^2} + V_{\bigcirc}(r,\theta), \end{aligned} \tag{4.1}$$

where the spacial coordinates $r_{\parallel}$ and $r_{\perp}$ correspond to the new cell coordinate system, *x*' and *y*', shown in Fig.8, and $\mu_i = \frac{m_i^e m_i^h}{m_i^e + m_i^h}$ are the reduced effective masses of the electron-hole system for each direction. This Hamiltonian is composed of three terms: two kinetic terms (first and second) and a potential term (third).

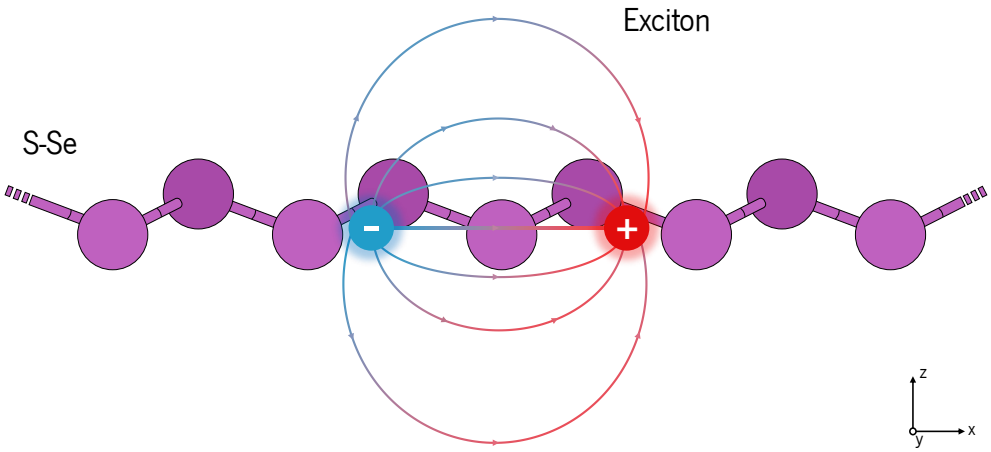


Figure 16: Stylised illustration of an exciton in square selenene

As shown in Chapter 3, the effective masses of electrons and holes in square selenene differ by an order of magnitude depending on the direction considered. To account for this strong anisotropy, the usual kinetic term -$\frac{\hbar^2}{2\mu}\nabla^2$ was split into $\parallel$ and $\perp$ components, each with their respective reduced mass $\mu_\parallel$ and $\mu_\perp$. To simplify the problem, the anisotropy of the kinetic term can be passed to the potential energy by considering the change of variables[61]

$$R_i = \sqrt{\frac{\mu_\parallel + \mu_\perp}{\mu}} r_i, \tag{4.2}$$

although this simplification does not offer much value due to the anisotropy of square selenene. The usual potential used to study excitons in 2D materials is the Rytova-Keldysh potential[62,63]

$$V_{RK}(r) = -\frac{e^2}{4\pi\epsilon_0}\frac{\pi}{2}\frac{1}{r_0}\left[H_0\left(\frac{\kappa r}{r_0}\right) - Y_0\left(\frac{\kappa r}{r_0}\right)\right], \tag{4.3}$$

where $\kappa = \frac{\epsilon_1+\epsilon_2}{2}$ is the mean dielectric function of the media that surrounds the 2D material, r_0 is the screening length, $H_0(x)$ is the Struve function of the zeroth order and $Y_0(x)$ is the Bessel function of the zeroth order of the second kind. This Rytova-Keldysh potential is the solution of the electrostatics problem that consists of the electron-hole interaction inside a nano-sheet of permittivity ϵ and thickness d, while being surrounded by media of permittivities ϵ_1 and ϵ_2.

However, as per our calculations, the screening length of square selenene depends on the direction considered, with $r_{0\parallel} \approx 3r_{0\perp}$, calling for a different potential. The treatment of this case is done by Kamban *et al.*[7], which we replicate (see Appendix C), to obtain the last term of Eq.(4.1) - $V_{Q}(r,\theta)$. We further approximate this term and find the energy functional associated with the effective Hamiltonian, using a simple normalised trial excitonic wavefunction that takes into account anisotropy[64], which has the form

$$\phi(r_\parallel, r_\perp) = \sqrt{\frac{2}{\pi\lambda_\parallel\lambda_\perp}} e^{-\sqrt{\left(\frac{r_\parallel}{\lambda_\parallel}\right)^2 + \left(\frac{r_\perp}{\lambda_\perp}\right)^2}}, \tag{4.4}$$

where $\lambda_\parallel, \lambda_\perp$ are variational parameters with dimension of length.

Finally, we simplify the energy functional until it only contains integrals in the polar coordinate θ and minimise it numerically to find the exciton ground state binding energy and wavefunction.

4.1 Interaction energy approximation

The first step in our journey to probe for excitonic states in square selenene is to find an approximate form of the interaction energy given by[7], in SI units

$$V_{\bigcirc}(r,\theta) = -\frac{e^2}{4\pi\epsilon_0}\left[\underbrace{\int_0^\infty \frac{J_0(qr)}{\sqrt{\epsilon_\parallel \epsilon_\perp}}dq}_{\equiv V_r(r)} + 2\underbrace{\sum_{k=1}^{\infty}\cos(2k\theta)\int_0^\infty \frac{1}{\sqrt{\epsilon_\parallel\epsilon_\perp}}\left(\frac{\sqrt{\epsilon_\parallel}-\sqrt{\epsilon_\perp}}{\sqrt{\epsilon_\parallel}+\sqrt{\epsilon_\perp}}\right)^k J_{2k}(qr)dq}_{\equiv V_\theta(r,\theta)}\right], \tag{4.5}$$

where $\parallel$ and $\perp$ refer to the zigzag and armchair directions in real space[1], respectively, $\epsilon_i = \kappa + r_{0i}q$ and J_n is the n^{th} order Bessel function of the first kind. For simplicity, we considered a free-standing sheet of square selenene, which implies $\kappa = 1$. We also note that when $r_{0\parallel}{=}r_{0\perp}$, we recover the Rytova-Keldysh potential[7].

In the following subsections, we approximate $V_{\bigcirc}(r,\theta)$ to alleviate the computational workload when using the variational method, as well as to avoid the numerical calculation of improper integrals with highly oscillatory kernels.

4.1.1 Radial term

We start with the radial term, given by

$$\begin{aligned} V_r(r) &= \int_0^\infty \frac{J_0(qr)}{\sqrt{\epsilon_\parallel\epsilon_\perp}}dq \\ &= \int_0^\infty \frac{J_0(qr)}{\sqrt{(1+r_{0\parallel}q)(1+r_{0\perp}q)}}dq \\ &\equiv \int_0^\infty f(q)J_0(qr)dq. \end{aligned} \tag{4.6}$$

To find an approximate closed form for this integral, we approximate $f(q)$ as

$$f(q) \approx \frac{1+q\bar{r}}{(1+r_{0\parallel}q)(1+r_{0\perp}q)}, \tag{4.7}$$

where $\bar{r}$ is the geometric mean of the screening lengths, given by

$$\bar{r} = \sqrt{r_{0\parallel}r_{0\perp}}. \tag{4.8}$$

This results in a good approximation, with a maximum relative error of 6% from the numerically calculated values, as seen in Fig.(17) .

[1] Not to be confused with the parallel and perpendicular directions in reciprocal space.

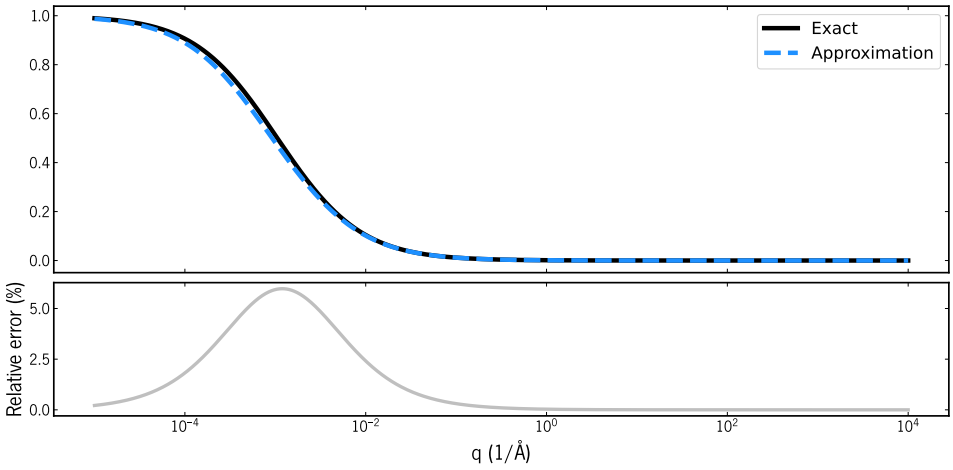


Figure 17: Exact (black line) vs approximation (coloured dashed line) of the function f(q) with relative percentage error (grey line). The curves were calculated using $r_{0\parallel}$= 1691.08 Å and $r_{0\perp}$= 455.25 Å.

This approximation allows us to evaluate the radial term as

$$
\begin{aligned}
V_r(r) &= \int_0^\infty f(q) J_0(qr)\, dq \\
&\approx \frac{1}{2(r_{0\parallel}-r_{0\perp})\bar{r}} \Bigg\{ 2 \underbrace{\left[(r_{0\perp}-\bar{r})\ {}_0F_1^{(1,0)}\left(1, \frac{-r^2}{4r_{0\parallel}^2}\right) + (\bar{r}-r_{0\parallel})\ {}_0F_1^{(1,0)}\left(1, \frac{-r^2}{4r_{0\perp}^2}\right) \right]}_{\equiv F(r)\ \text{(F-term)}} \\
&+ \underbrace{\left[(\bar{r}-r_{0\perp}) \ln\left(\frac{4r_{0\parallel}^2}{r^2}\right) J_0\left(\frac{r}{r_{0\parallel}}\right) + (r_{0\parallel}-\bar{r}) \ln\left(\frac{4r_{0\perp}^2}{r^2}\right) J_0\left(\frac{r}{r_{0\perp}}\right) \right]}_{\equiv \mathcal{J}(r)\text{(J-term)}} \\
&+ \pi \underbrace{\left[(\bar{r}-r_{0\perp}) H_0\left(\frac{r}{r_{0\parallel}}\right) + (r_{0\parallel}-\bar{r}) H_0\left(\frac{r}{r_{0\perp}}\right) \right]}_{\equiv \mathcal{H}(r)\ \text{(H-term)}} \Bigg\},
\end{aligned}
\tag{4.9}
$$

where ${}_0F_1^{(1,0)}(a,z) = \partial_a \left[{}_0F_1(a,z)/\Gamma(a) \right]$ is the derivative in respect to the parameter a of the regularised generalised hypergeometric function with $p = 0$ and $q = 1$, $J_0(x)$ denotes the zeroth order Bessel function of the first kind, and $H_0(x)$ the zeroth order Struve function. As shown in Fig.18, Eq.(4.9) yields a good approximation of $V_r(r)$, with a maximum relative error of 5%.

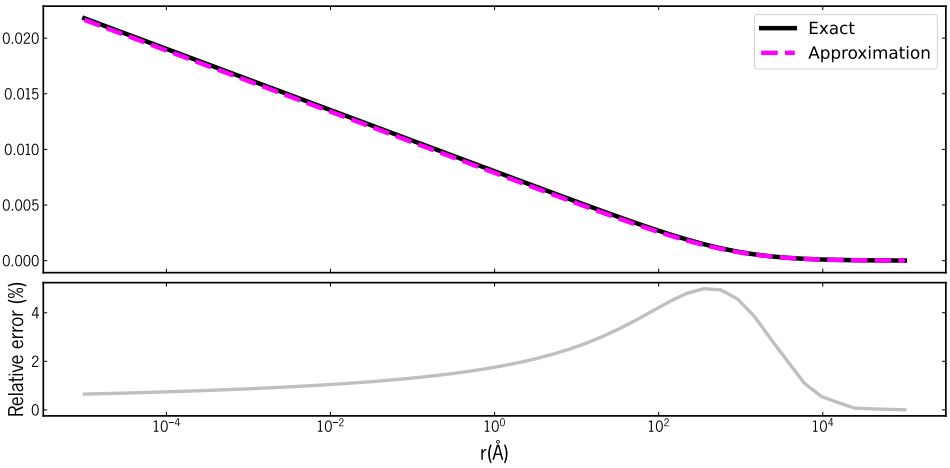


Figure 18: Numerical (black line) vs approximation (coloured dashed line) of $V_r(r)$ with relative percentage error (grey line). The curves where calculated using $r_{0\parallel}$= 1691.08 Å and $r_{0\perp}$= 455.25 Å.

4.1.2 Angular term

The angular term is given by

$$
\begin{aligned}
V_\theta(r,\theta) &= \sum_{k=1}^{\infty} \cos(2k\theta) \int_0^\infty \frac{1}{\sqrt{\epsilon_\parallel \epsilon_\perp}} \left(\frac{\sqrt{\epsilon_\parallel} - \sqrt{\epsilon_\perp}}{\sqrt{\epsilon_\parallel} + \sqrt{\epsilon_\perp}} \right)^k J_{2k}(qr)\,dq \\
&= \sum_{k=1}^{\infty} \cos(2k\theta) \int_0^\infty \frac{1}{\sqrt{(1+r_{0\parallel}q)(1+r_{0\perp}q)}} \left(\frac{\sqrt{1+r_{0\parallel}q} - \sqrt{1+r_{0\perp}q}}{\sqrt{1+r_{0\parallel}q} + \sqrt{1+r_{0\perp}q}} \right)^k J_{2k}(qr)\,dq \\
&\equiv \sum_{k=1}^{\infty} \cos(2k\theta) \underbrace{\int_0^\infty F_k(q) J_{2k}(qr)\,dq}_{\equiv v_k(r)} . \qquad (4.10)
\end{aligned}
$$

We approximate this angular contribution to the potential by fitting $v_k(r)$ for different k values. To do so, we must truncate the infinite sum at some K value. We chose K=7, since the inclusion of higher order terms in the sum will only alter the value by less than 0.02%. The fit function is given by

$$
v_{k,N}(r) = A_k + \frac{e^{-r/\bar{r}}}{\bar{r}} \sum_{n=0}^{N} B_{k,n} \left(r/\bar{r}\right)^n , \qquad (4.11)
$$

which substituted in Eq.(4.10) yields

$$
\begin{aligned}
V_\theta(r,\theta) &\approx V_\theta^{K,N}(r,\theta) \qquad (4.12) \\
&= \sum_{k=1}^{K} \cos(2k\theta) \left[A_k + \frac{e^{-r/\bar{r}}}{\bar{r}} \sum_{n=0}^{N} B_{k,n} \left(r/\bar{r}\right)^n \right] . \qquad (4.13)
\end{aligned}
$$

Considering $N = 20$ and $K = 7$ yields the results shown in Fig.19. This method offers an accurate description of the angular term, as it closely follows the numerical data. We note that the rising relative error, around 10^4Å , is due to $V_\theta^{K,N}$ decaying faster to zero than the numerically computed values.

The final form for the approximated interaction energy is given by[2]

$$V_{\bullet}(r,\theta) \approx -\frac{e^2}{4\pi\epsilon_0}\frac{1}{2(r_{0\|}-r_{0\perp})\bar{r}}\left[2\mathcal{F}(r)+\mathcal{J}(r)+\pi\mathcal{H}(r)\right]-\frac{e^2}{4\pi\epsilon_0}2\sum_{k=1}^{K}\cos(2k\theta)v_\theta^{K,N}(r,\theta), \tag{4.14}$$

where we compare it to the numerically calculated values for different angles, as shown in Fig.20.

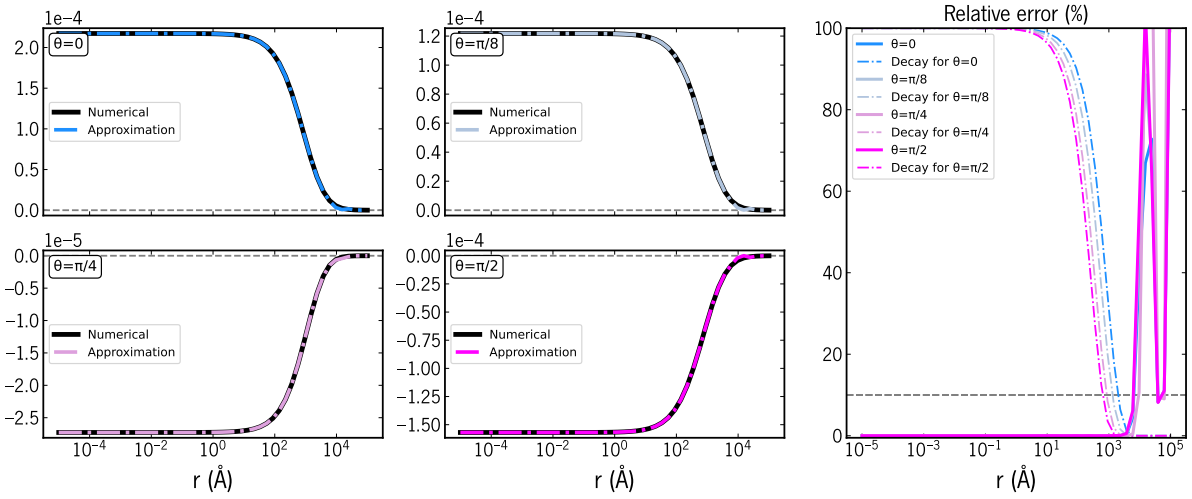


Figure 19: Numerical (black lines) vs approximation (dashed coloured lines) of $V_\theta(r,\theta)$ for different angles (4 left panels), relative percentage error (large right panel: coloured lines) and decay lines of the square modulus of the trial wavefunction renormalised to 100 (large right panel: dash-dotted coloured lines). The curves were calculated using $r_{0\|}$= 1691.08 Å, $r_{0\perp}$= 455.25 Å, $\lambda_\|$=1587.5 Å, and $\lambda_\perp$=653.13 Å.

We obtained a satisfactory description of the angular potential with a maximum relative error of $\approx$ 25% in the $\theta = 0$ direction. We note that the potential term enters the excitonic energy functional as

$$V[\phi] = \int |\phi(r,\theta)|^2 V_{\bullet}(r,\theta) d^2r, \tag{4.15}$$

where ϕ is the trial excitonic wavefunction. The decay of $|\phi|^2$ will mitigate the error. As a comparison, we added the decay lines, for each angle, of the square modulus of the trial wavefunction, given by Eq.(4.4), renormalised to 100 in Fig.19 and Fig.20. The variational parameters used are the ones that minimise the

[2] See Eq.(4.9) for the definitions of $\mathcal{F}(r)$, $\mathcal{J}(r)$ and $\mathcal{H}(r)$.

excitonic energy functional when considering this approximation, which will be calculated later in Section 4.2. They show that the error of our approximation is diminished by the decay of the wavefunction

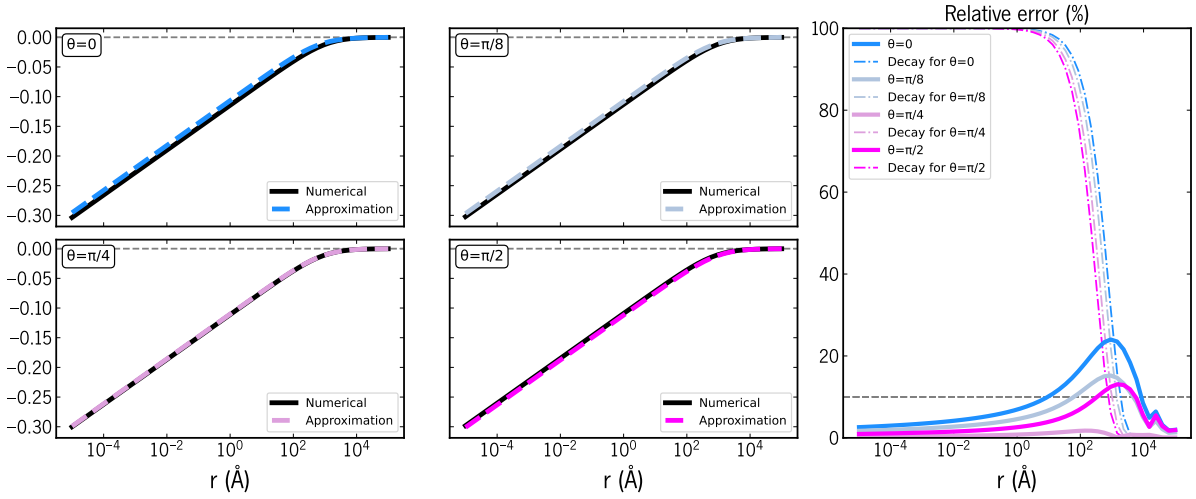


Figure 20: Numerical (black lines) vs approximation (dashed coloured lines) of $V_{\bigcirc}(r,\theta)$ for different angles (4 left panels), relative percentage error (large right panel: coloured lines) and decay lines of the square modulus of the trial wavefunction renormalised to 100 (large right panel: dash-dotted coloured lines). The curves were calculated using $r_{0\parallel}$= 1691.08 Å, $r_{0\perp}$= 455.25 Å, $\lambda_{\parallel}$=1587.5 Å, and $\lambda_{\perp}$=653.13 Å.

4.2 Energy functional

Having found an approximation to the potential $V_{\bigcirc}(r,\theta)$, we want to apply the variational method to the following problem

$$H_{\bigcirc}\phi(r_{\parallel}, r_{\perp}) = E_{\bigcirc}\phi(r_{\parallel}, r_{\perp}), \tag{4.16}$$

where $H_{\bigcirc}$ and $\phi(r,\theta)$ are given by Eq.(4.1) and Eq.(4.4), respectively. The variational theorem states that

$$\mathcal{E}_{\bigcirc}[\phi] \geq E_0^{\bigcirc}, \tag{4.17}$$

where $\mathcal{E}_{\bigcirc}[\phi]$ is the energy functional and $E_0^{\bigcirc}$ is the actual exciton ground state energy. We must minimise the energy functional, given by (taking into account that our trial wavefunction is normalised)

$$\mathcal{E}_{\bigcirc}[\phi] = \langle\phi|H_{\bigcirc}|\phi\rangle\,, \tag{4.18}$$

which, in the real space representation, is written as

$$\mathcal{E}_{\bigcirc}[\phi] = \underbrace{-\frac{\hbar^2}{2}\left[\frac{1}{\mu_{\parallel}}\int \phi(r_{\parallel}, r_{\perp})\frac{\partial^2}{\partial r_{\parallel}^2}\phi(r_{\parallel}, r_{\perp})d^2r + \frac{1}{\mu_{\perp}}\int \phi(r_{\parallel}, r_{\perp})\frac{\partial^2}{\partial r_{\perp}^2}\phi(r_{\parallel}, r_{\perp})d^2r\right]}_{T_{\parallel}+T_{\perp}\text{ (Kinetic terms)}}$$
$$+ \underbrace{\int |\phi|^2 V_{\bigcirc}(r,\theta)d^2r}_{V\text{ (Potential term)}}. \tag{4.19}$$

In the following parts, we find a closed form for the kinetic terms and simplify the potential term until we are only left with angular integrals.

4.2.1 Kinetic terms

In this subsection, we derive the form of the kinetic term associated with $r_{\parallel}$. For $r_{\perp}$ we just need to interchange $\mu_{\parallel} \leftrightarrow \mu_{\perp}$ and $\lambda_{\parallel} \leftrightarrow \lambda_{\perp}$ in the final result. The first kinetic term is given by

$$T_{\parallel} = -\frac{\hbar^2}{2\mu_{\parallel}} \frac{2}{\pi\lambda_{\parallel}\lambda_{\perp}} \int e^{-\sqrt{\left(\frac{r_{\parallel}}{\lambda_{\parallel}}\right)^2+\left(\frac{r_{\perp}}{\lambda_{\perp}}\right)^2}} \left(\frac{\partial^2}{\partial r_{\parallel}^2} e^{-\sqrt{\left(\frac{r_{\parallel}}{\lambda_{\parallel}}\right)^2+\left(\frac{r_{\perp}}{\lambda_{\perp}}\right)^2}} \right) d^2r \tag{4.20}$$

$$= C \int e^{-\sqrt{\left(\frac{r_{\parallel}}{\lambda_{\parallel}}\right)^2+\left(\frac{r_{\perp}}{\lambda_{\perp}}\right)^2}} \frac{\left(\lambda_{\parallel}^2\lambda_{\perp}^2 r_{\parallel}^2 r_{\perp}^2 - \lambda_{\parallel}^4\lambda_{\perp}^2 r_{\perp}^2 \sqrt{\left(\frac{r_{\parallel}}{\lambda_{\parallel}}\right)^2+\left(\frac{r_{\perp}}{\lambda_{\perp}}\right)^2} + \lambda_{\perp}^4 r_{\parallel}^4 \right)}{\left(\lambda_{\parallel}\lambda_{\perp}^2 r_{\parallel}^2 + \lambda_{\parallel}^3 r_{\perp}^2\right)^2} d^2r \tag{4.21}$$

$$= C\frac{(\lambda_{\parallel}\lambda_{\perp})^5}{(\lambda_{\parallel}^3\lambda_{\perp}^2)^2} \left[\int_{-\infty}^{\infty}\int_{-\infty}^{\infty} e^{-2\sqrt{x^2+y^2}} \frac{x^2y^2}{\left(x^2+y^2\right)^2} dxdy - \int_{-\infty}^{\infty}\int_{-\infty}^{\infty} e^{-2\sqrt{x^2+y^2}} \frac{y^2\sqrt{x^2+y^2}}{\left(x^2+y^2\right)^2} dxdy \right.$$
$$\left. + \int_{-\infty}^{\infty}\int_{-\infty}^{\infty} e^{-2\sqrt{x^2+y^2}} \frac{x^4}{\left(x^2+y^2\right)^2} dxdy \right] \tag{4.22}$$

$$= C\frac{\lambda_{\perp}}{\lambda_{\parallel}} \left[\int_0^{2\pi} d\varphi \cos^2(\varphi) \sin^2(\varphi) \int_0^{\infty} d\rho e^{-2\rho}\rho - \int_0^{2\pi} d\varphi \sin^2(\varphi) \int_0^{\infty} d\rho e^{-2\rho} \right.$$
$$\left. + \int_0^{2\pi} d\varphi \cos^4(\varphi) \int_0^{\infty} d\rho e^{-2\rho}\rho \right] \tag{4.23}$$

$$= -\frac{\hbar^2}{2\mu_{\parallel}} \frac{2}{\pi\lambda_{\parallel}\lambda_{\perp}} \left[\frac{\pi}{16} - \frac{\pi}{2} + \frac{3\pi}{16} \right] \frac{\lambda_{\perp}}{\lambda_{\parallel}}$$

$$= \frac{1}{\mu_{\parallel}} \left(\frac{\hbar}{2\lambda_{\parallel}} \right)^2, \tag{4.24}$$

where we performed the following actions between steps

- (4.20)→(4.21): $C \equiv -\frac{\hbar^2}{2\mu_{\parallel}} \frac{2}{\pi\lambda_{\parallel}\lambda_{\perp}}$.
- (4.21)→(4.22): Variable substitution $r_{\parallel}/\lambda_{\parallel} = x$ and $r_{\perp}/\lambda_{\perp} = y$.
- (4.22)→(4.23): Switch to polar coordinates (ρ, φ).

So, the sum of the kinetic terms is given by

$$T_{\parallel} + T_{\perp} = \left(\frac{\hbar}{2}\right)^2 \left[\frac{1}{\mu_{\parallel}\lambda_{\parallel}^2} + \frac{1}{\mu_{\perp}\lambda_{\perp}^2} \right], \tag{4.25}$$

which reduces to $\frac{\hbar^2}{2\mu\lambda^2}$ in the isotropic case.

4.2.2 Potential term

The potential part of the functional is broken down into 4 integrals, 3 named by the terms in Eq.(4.9) and one angular contribution

$$
\begin{aligned}
V &= \int \left|\phi^2\right| V_{\bullet}(r,\theta)\, d^2 r \\
&\approx -\frac{e^2}{4\pi\epsilon_0}\frac{2}{\pi\lambda_{\parallel}\lambda_{\perp}}\left[2\underbrace{\int_0^{2\pi} d\theta \int_0^{\infty} dr\, e^{-2rp(\theta)} r\mathcal{F}(r)}_{\text{F-integral}} + \underbrace{\int_0^{2\pi} d\theta \int_0^{\infty} dr\, e^{-2rp(\theta)} r\mathcal{J}(r)}_{\text{J-integral}}\right. \\
&\left. + \pi\underbrace{\int_0^{2\pi} d\theta \int_0^{\infty} dr\, e^{-2rp(\theta)} r\mathcal{H}(r)}_{\text{H-integral}} + 2\underbrace{\int_0^{2\pi} d\theta \int_0^{\infty} dr\, r e^{-2rp(\theta)} V_{\theta}^{K,N}(r,\theta)}_{\text{Angular term integral}}\right].
\end{aligned} \tag{4.26}
$$

We rewrote the trial wavefunction in polar coordinates - $r_{\parallel}, r_{\perp} \to r, \theta$ - and defined

$$
p(\theta, \lambda_{\parallel}, \lambda_{\perp}) = \sqrt{\frac{\cos^2(\theta)}{\lambda_{\parallel}^2} + \frac{\sin^2(\theta)}{\lambda_{\perp}^2}}, \tag{4.27}
$$

where we note that, to alleviate the notation, we wrote $p(\theta, \lambda_{\parallel}, \lambda_{\perp})$ as $p(\theta)$. In the following subsections, we simplify these integrals by evaluating the radial parts to ease numerical implementation and reduce computational cost.

F-integral

The F-integral is given by

$$
\begin{aligned}
I_F = (r_{0\perp} - \bar{r}) &\int_0^{2\pi} d\theta \int_0^{\infty} r\, dr\, e^{-2rp(\theta)}\, {}_0F_1^{(1,0)}\left(1, -\frac{r^2}{4r_{0\parallel}^2}\right) \\
+ (\bar{r} - r_{0\parallel}) &\int_0^{2\pi} d\theta \int_0^{\infty} r\, dr\, e^{-2rp(\theta)}\, {}_0F_1^{(1,0)}\left(1, -\frac{r^2}{4r_{0\perp}^2}\right).
\end{aligned} \tag{4.28}
$$

We focus on the radial integral with $r_{0\parallel}, r_{0\perp} \to r_{0i}$, which yields[3]

$$
\begin{aligned}
&\int_0^{\infty} r\, dr\, e^{-2rp(\theta)}\, {}_0F_1^{(1,0)}\left(1, -\frac{r^2}{4r_{0i}^2}\right) = \frac{1}{4\left(\lambda_{\parallel}^2\left(\lambda_{\perp}^2 + 4r_{0i}^2\sin^2\theta\right) + 4\lambda_{\perp}^2 r_{0i}^2\cos^2\theta\right)^2} \\
&\left\{(\lambda_{\parallel}\lambda_{\perp} r_{0i})^2\sqrt{\frac{1}{p(\theta)^2 r_{0i}^2} + 4}\left[\sqrt{\frac{1}{p(\theta)^2 r_{0i}^2} + 4}\left(2r_{0i}^2\left(\cos(2\theta)\left(\lambda_{\perp}^2 - \lambda_{\parallel}^2\right) + \lambda_{\perp}^2 + \lambda_{\parallel}^2\right)\right.\right.\right. \\
&{}_2F_1^{(0,0,1,0)}\left(-\frac{1}{2}, 1, 1, -\frac{1}{4p(\theta)^2 r_{0i}^2}\right) - (\lambda_{\parallel}\lambda_{\perp})^2\, {}_2F_1^{(0,0,1,0)}\left(\frac{1}{2}, 1, 1, -\frac{1}{4p(\theta)^2 r_{0i}^2}\right)\Bigg) \\
&\left.\left.+(2\lambda_{\parallel}\lambda_{\perp})^2 + 8\gamma r_{0i}^2\left(\lambda_{\parallel}^2\sin^2\theta + \lambda_{\perp}^2\cos^2\theta\right)\right]\right\} \equiv F_r^i(\theta),
\end{aligned} \tag{4.29}
$$

[3] The trick to evaluate this integral in Mathematica is to pull out the derivative with respect to the parameter a, integrate, and then derivate.

where ${}_2F_1^{(n_a,n_b,n_c,n_n)} = \frac{\partial^{n_a}}{\partial a^{n_a}}\frac{\partial^{n_b}}{\partial b^{n_b}}\frac{\partial^{n_c}}{\partial a^{n_c}}\frac{\partial^{n_z}}{\partial a^{n_z}}\left[{}_2F_1(a,b,c,z)\right]$, ${}_2F_1(a,b,c,z)$ is the ordinary hypergeometric function, and $\gamma \approx 0.5772$ is the Euler–Mascheroni constant. With this, the F-integral becomes

$$\begin{aligned} I_F &= (r_{0\perp} - \bar{r}) \int_0^{2\pi} d\theta F_r^{\parallel}(\theta) + (\bar{r} - r_{0\parallel}) \int_0^{2\pi} d\theta F_r^{\perp}(\theta) \\ &\equiv (r_{0\perp} - \bar{r}) I_F^{\parallel}(\lambda_{\parallel}, \lambda_{\perp}) + (\bar{r} - r_{0\parallel}) I_F^{\perp}(\lambda_{\parallel}, \lambda_{\perp}), \end{aligned} \tag{4.30}$$

where we remind the dependence on the variational parameters, which were hidden inside $p(\theta)$ to simplify the notation.

J-integral

The J-integral is given by

$$\begin{aligned} I_J = (\bar{r} - r_{0\perp}) \int_0^{2\pi} d\theta \int_0^{\infty} r\, dr\, e^{-2rp(\theta)} \ln\left(\frac{4r_{0\parallel}^2}{r^2}\right) J_0\left(\frac{r}{r_{0\parallel}}\right) \\ + (r_{0\parallel} - \bar{r}) \int_0^{2\pi} d\theta \int_0^{\infty} r\, dr\, e^{-2rp(\theta)} \ln\left(\frac{4r_{0\perp}^2}{r^2}\right) J_0\left(\frac{r}{r_{0\perp}}\right). \end{aligned} \tag{4.31}$$

As before, we focus on the generalised radial integral ($r_{0\parallel}, r_{0\perp} \to r_{0i}$), obtaining

$$\begin{aligned} \int_0^{\infty} r\, dr\, e^{-2rp(\theta)} \ln\left(\frac{4r_{0i}^2}{r^2}\right) J_0\left(\frac{r}{r_{0i}}\right) = -\frac{1}{4\pi^2}\Bigg\{ {}_2F_1^{(0,1,0,0)}\left(1, \frac{3}{2}, 1, -\frac{1}{4p(\theta)^2 r_{0i}^2}\right) \\ + {}_2F_1^{(1,0,0,0)}\left(1, \frac{3}{2}, 1, -\frac{1}{4p(\theta)^2 r_{0i}^2}\right) - \frac{16\left[\ln(4p(\theta)r_{0i}) + \gamma - 1\right]}{\left(\frac{1}{p(\theta)^2 r_{0i}^2} + 4\right)^{\frac{3}{2}}} \Bigg\} \equiv \mathcal{J}_r^i(\theta), \end{aligned} \tag{4.32}$$

which allows us to rewrite Eq.(4.31) as

$$\begin{aligned} I_J &= (\bar{r} - r_{0\perp}) \int_0^{2\pi} d\theta \mathcal{J}_r^{\parallel}(\theta) + (r_{0\parallel} - \bar{r}) \int_0^{2\pi} d\theta \mathcal{J}_r^{\perp}(\theta) \\ &\equiv (\bar{r} - r_{0\perp}) I_J^{\parallel}(\lambda_{\parallel}, \lambda_{\perp}) + (r_{0\parallel} - \bar{r}) I_J^{\perp}(\lambda_{\parallel}, \lambda_{\perp}). \end{aligned} \tag{4.33}$$

H-integral

The last term of the radial part of the potential is the H-integral, given by

$$I_H = \pi(\bar{r} - r_{0\perp}) \int_0^{2\pi} d\theta \int_0^{\infty} r\, dr\, e^{-2rp(\theta)} H_0\left(\frac{r}{r_{0\parallel}}\right) + \pi(r_{0\parallel} - \bar{r}) \int_0^{2\pi} d\theta \int_0^{\infty} r\, dr\, e^{-2rp(\theta)} H_0\left(\frac{r}{r_{0\perp}}\right). \tag{4.34}$$

Once again, we evaluate the integral in r for the general case (r_{0i})

$$\int_0^\infty r\,dr\,e^{-2rp(\theta)}H_0\left(\frac{r}{r_{0i}}\right)=\frac{1}{\pi p(\theta)}\left\{\frac{r_{0i}}{\left[2r_{0i}p(\theta)\right]^2+1}+\frac{4p(\theta)^2r_{0i}^3\,\mathrm{csch}^{-1}\left[2p(\theta)r_{0i}\right]}{\left\{\left[2r_{0i}p(\theta)\right]^2+1\right\}^{\frac{3}{2}}}\right\}\equiv\mathcal{H}_r^i(\theta), \tag{4.35}$$

from which we get

$$\begin{aligned} I_H &= \pi(\bar{r}-r_{0\perp})\int_0^{2\pi}d\theta\mathcal{H}_r^{\parallel}(\theta)+\pi(r_{0\parallel}-\bar{r}\,)\int_0^{2\pi}d\theta\mathcal{H}_r^{\perp}(\theta)\\ &\equiv \pi(\bar{r}-r_{0\perp})I_H^{\parallel}(\lambda_\parallel,\lambda_\perp)+\pi(r_{0\parallel}-\bar{r}\,)I_{\mathrm{H}}^{\perp}(\lambda_\parallel,\lambda_\perp). \end{aligned} \tag{4.36}$$

Angular term integral

Considering our approximation of the angular part of the potential, given by Eq.(4.13), we have

$$\begin{aligned} &\sum_{k=1}^{K}\int_0^{2\pi}d\theta\cos(2k\theta)\int_0^\infty dr\,re^{-2rp(\theta)}\left[A_k+\frac{e^{-r/\bar{r}}}{\bar{r}}\sum_{n=0}^{N}B_{\mathrm{k,n}}\left(r/\bar{r}\right)^n\right]\\ &=\sum_{k=1}^{K}\int_0^{2\pi}d\theta\cos(2k\theta)\int_0^\infty dr\left\{re^{-2rp(\theta)}A_k+e^{-r\left[2p(\theta)+\frac{1}{\bar{r}}\right]}\sum_{n=0}^{N}B_{\mathrm{k,n}}\left(r/\bar{r}\right)^{n+1}\right\}\\ &=\sum_{k=1}^{K}\int_0^{2\pi}d\theta\cos(2k\theta)\left\{\sum_{n=0}^{N}\frac{(n+1)!}{\bar{r}^{\,n+1}}\frac{B_{k,n}}{\left[2p(\theta)+\frac{1}{\bar{r}}\right]^{n+2}}+\frac{A_k}{4p(\theta)^2}\right\}\equiv \mathrm{I}_{V_\theta}^{K,N}(\lambda_\parallel,\lambda_\perp), \end{aligned} \tag{4.37}$$

where we evaluated the radial integral.

4.2.3 Final energy functional

The final energy functional is obtained by considering Eq.(4.25), substituting Eq.(4.30), Eq.(4.33), Eq.(4.36), and adding Eq.(4.26), after substituting Eq.(4.37), which yields

$$\begin{aligned} \mathcal{E}^{(K,N)}(\lambda_\parallel,\lambda_\perp) &= T_\parallel+T_\perp+E_r+E_\theta\\ &=\frac{2}{\pi\lambda_\parallel\lambda_\perp}\left\{\pi\left(\frac{\hbar}{2}\right)^2\left[\frac{\lambda_\perp}{\mu_\parallel\lambda_\parallel}+\frac{\lambda_\parallel}{\mu_\perp\lambda_\perp}\right]\right.\\ &\left.-\frac{e^2}{4\pi\epsilon_0}\frac{1}{2(r_{0\parallel}-r_{0\perp})\bar{r}}\left[(\bar{r}-r_{0\perp})\left(I_J^{\parallel}(\lambda_\parallel,\lambda_\perp)+\pi I_H^{\parallel}(\lambda_\parallel,\lambda_\perp)-2I_F^{\parallel}(\lambda_\parallel,\lambda_\perp)\right)\right.\right. \end{aligned}$$

$$+(r_{0\parallel}-\bar{r})\left(I_J^{\perp}(\lambda_\parallel,\lambda_\perp)+\pi I_H^{\perp}(\lambda_\parallel,\lambda_\perp)-2I_F^{\perp}(\lambda_\parallel,\lambda_\perp)\right)\Big]+\frac{e^2}{4\pi\epsilon_0}I_{V_\theta}^{(K,N)}(\lambda_\parallel,\lambda_\perp)\Bigg\}, \tag{4.38}$$

where we separated the potential energy into radial and angular contributions, E_r and E_θ respectively. The only instances of the variational parameters are $\lambda_\parallel\lambda_\perp$,$\lambda_\parallel^2$ and $\lambda_\perp^2$, hence the functional respects

$$\mathcal{E}_{\bigcirc}(\lambda_\parallel,\lambda_\perp)=\mathcal{E}_{\bigcirc}(-\lambda_\parallel,-\lambda_\perp)\quad\wedge\quad\mathcal{E}_{\bigcirc}(-\lambda_\parallel,\lambda_\perp)=\mathcal{E}_{\bigcirc}(\lambda_\parallel,-\lambda_\perp), \tag{4.39}$$

which allows us to limit our search to the first and fourth quadrant of the variational parameter space $\{\lambda_\parallel,\lambda_\perp\}$. We minimised the functional, given by Eq.(4.38), considering three sets of effective masses (see Table.5). The minimised energy, decomposed into contributions, as well as the corresponding variational parameters, are shown in Table.7.

Table 7: Variational parameters $(\lambda_\parallel,\lambda_\perp)$ of the trial excitonic wavefunction that minimise the energy functional for three different sets of effective masses. The resulting energies ($E_{\bigcirc}$) are decomposed into kinetic (T), radial (E_r) and angular contributions (E_θ).

Effective masses	$\lambda_\parallel$(Å)	$\lambda_\perp$(Å)	$E_{\bigcirc}$ (meV)		
			T	E_r	E_θ
Effective model	1587.5	653.13	-23.89		
			7.31	-31.2	-1.63×10^{-3}
PAOFLOW	1562.5	643.87	-24.17		
			7.25	-31.4	-1.62×10^{-3}
Lin *et al.*[8]	937.5	468.75	-31.78		
			5.758	-37.54	-1.29×10^{-3}

The values obtained using the two sets of effective masses from PAOFLOW and our effective model are quite similar, while the ones obtained using the effective masses from the work of Lin *et al.*[8] show a more strongly bound exciton. We note that in all cases the angular contribution to the binding energy is negligible ($\sim1\mu$eV).

Next, we point out that the ratios between the excitonic binding energy (E_b=$E_{\bigcirc}$), in square selenene, and the energy bandgap (E_g) are between 0.23 and 0.3, depending on the effective masses. These values

seem to respect the robust linear scaling law, studied by Jiang *et al.*[60], in two-dimensional semiconductors, which states that

$$E_b \approx 0.27 E_g. \tag{4.40}$$

This relation was also reported in earlier works[65]; however, they implied a non-zero exciton binding energy when no gap existed, which goes against the fundamental physics that describes excitons, as commented on by Zhang *et al.*[66]. We compiled the raw data from seven works[60,65–70] that deal with this linear relation and represented it in Fig.21, adding the point[4] for square selenene. However, there is a caveat: the scaling rule proposed by Jiang *et al.*[60] is based on GW calculations, which typically corrects the bandgap from DFT to larger values. It is not possible to quantitatively predict how this would affect the ratio for square selenene, since E_g, the effective masses, and the effective screening lengths would all be altered when considering GW calculations. It is relevant to note that Jian *et al.*[60] arrived at a slightly different linear relation, considering conventional $k\cdot$p perturbation theory and the hydrogen-like model of excitons, so it is possible that our treatment captures the physics behind this scaling law.

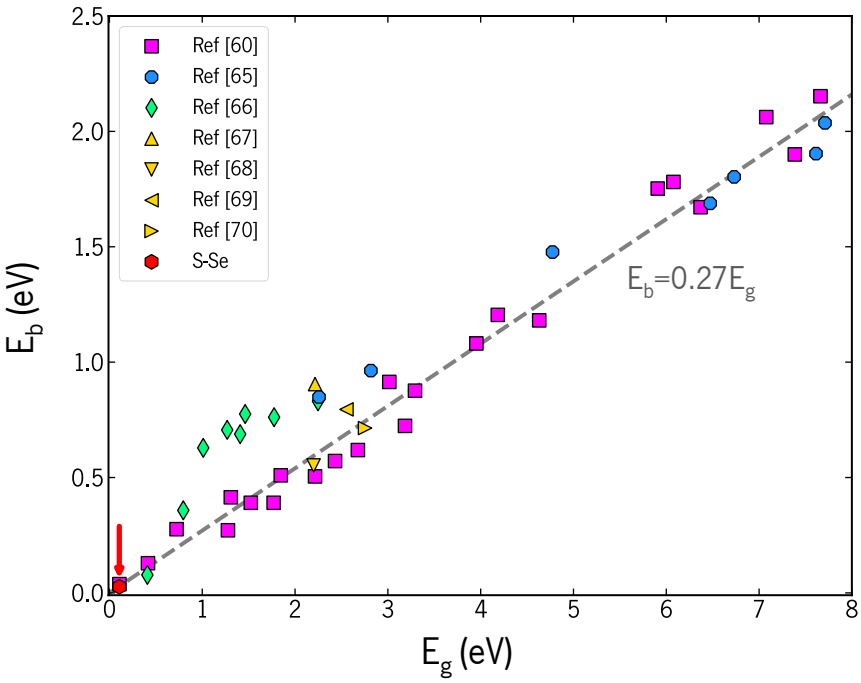


Figure 21: Compilation of exciton binding energies and band gaps of various 2D semiconductors, from different works.

A property of excitons inside a narrow-gapped material is the large spatial extension of the exciton

[4] Due to the scale considered in Fig.21 the different points for square selenene are undistinguishable, so we decided to only plot the point calculated using the effective masses from PAOFLOW.

wavefunction. The larger the gap is, the weaker the screening, as Eq.(3.12) shows, which results in a smaller exciton radius and higher binding energy. For square selenene, we have the opposite: a small gap leads to strong screening, which creates a large exciton radius with a small binding energy. To quantify the "size" of the exciton, we compute the root-mean-square (rms) distances, given by

$$L_j = \langle r_j^2 \rangle, \tag{4.41}$$

where the index j represents the directions ($\parallel$ or $\perp$). For our trial wavefunction, they take the simple form

$$L_j = \frac{\sqrt{3}}{2}\lambda_j, \tag{4.42}$$

where λ_j are the variational parameters defined in Eq.(4.4). In Table.8, we list these lengths for our minimised wavefunction parameters as well as other materials for comparison. The values for the effective masses from the work of Lin *et al.*[8] are appreciably smaller, especially in the $\parallel$-direction, but remain consistent with the values obtained using the effective masses from PAOFLOW. For comparison, the same lengths are shown for phosphorene, which possesses a much bigger gap. As a consequence, the excitonic wavefunction is much more localised, having values for L_j, two orders of magnitude smaller than the ones we derived for square selenene.

The root-mean-square we obtained for the ground excitonic state is not typical for 2D semiconductors, which tend to have a root-mean-square radius of $\approx$1-10 nm[71,72]. We note that the exciton Bohr radius, defined by

$$a_x = \frac{4\pi\epsilon\hbar^2}{\mu e^2}, \tag{4.43}$$

where ϵ is the dielectric constant and $\mu = \frac{m_e m_h}{m_e + m_h}$ is the electron-hole reduced mass, takes a value for InSb[73]- a 3D material with similar gap E_g=0.17 eV - of the same order of magnitude as the rms distances for square selenene. Although the excitonic Bohr radius is not the same quantity as L_j and InSb is a 3D crystal, the comparison serves to illustrate that excitons with large spatial extensions can exist for narrow gaps ($\sim$0.1 eV).

Finally, to illustrate the anisotropic nature of excitons in square selenene, we show the wavefunctions of the excitons, obtained using the effective masses from PAOFLOW and the work of Lin *et al.*[8] in Fig.22.

Table 8: Characteristic lengths of excitons in square selenene (source of the effective masses in parentheses), phosphorene, and InSb (3D). a_x is the excitonic Bohr radius.

	E_g (eV)	$L_{\parallel}$ (nm)	$L_{\perp}$ (nm)	a_X (nm)
S-Se (PAOFLOW)	0.106	135	55.8	-
S-Se (Lin *et al.*[8])	0.112	81.2	40.6	-
Phosphorene[74]	1.88	0.78	0.39	-
InSb[73]	0.17	-	-	65.6

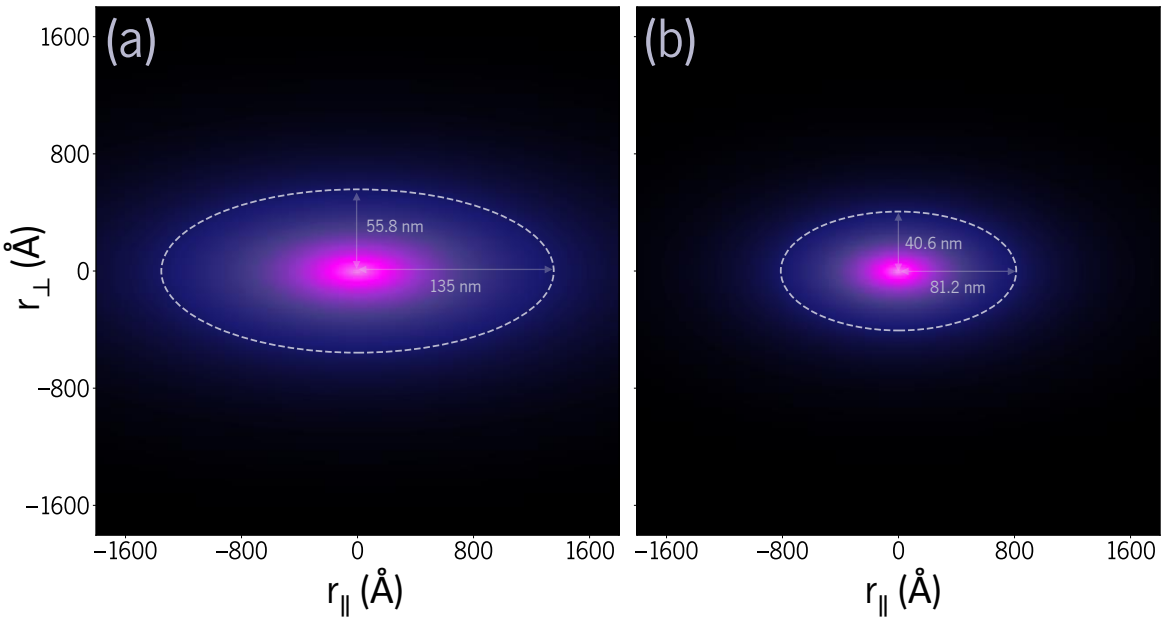


Figure 22: Square modulus of the ground state excitonic wavefunction in square selenene, obtained using the effective masses from: (a) PAOFLOW, (b) Lin *et al.*[8]. The white dashed lines represent ellipses whose semi-major and semi-minor axes are the characteristic lengths L_j, which are the root-mean-square radius of the excitonic wavefunction.

Chapter 5

Conclusion, Limitations and Further Work

In this thesis, we investigated the electronic and excitonic properties of square selenene (s-Se), a two-dimensional allotrope of selenium characterised by its strong anisotropic features, such as carrier mobilities, dispersion, and effective masses.

In Chapter 2, we explored the electronic properties of s-Se using Density Functional Theory. We obtained the band structure across the full Brillouin zone, for non- and fully relativistic calculations, which is in accordance with previous works, except for an additional splitting of the bands at the bandgap. Additionally, we computed the reciprocal space spin texture, i.e, the mean value of the spin operators across the Brillouin zone, and uncovered interesting spin patterns, such as spin-momentum locking, further adding to the characterisation of the electronic properties of square selenene. Finally, we demonstrated the presence of edge states in two types of s-Se nanoribbons ($\approx$10 nm wide), by analysing the contribution of states to the charge density.

In Chapter 3, we constructed an effective Hamiltonian that accurately describes the bandgap obtained from fully relativistic data. The cornerstone was a $k{\cdot}p$ Hamiltonian from the literature, to which we added two spin-orbit coupling (SOC) terms: an intrinsic SOC term and a modified version of the Rashba Hamiltonian. This suggests the presence of Rashba-like spin-orbit effects in s-Se, which is reinforced by the similarities in the spin-texture[51]. We then extracted the effective masses of electrons and holes along different directions, both from our effective model and from PAOFLOW's real-space tight-binding Hamiltonian, finding agreement with the literature. Finally, it also allowed us to easily estimate the effective screening lengths of s-Se without resorting to more advanced *ab initio* calculations.

Finally, in Chapter 4, we studied the formation of excitons in square selenene using an effective Hamiltonian that took into account its highly anisotropic features. The usual kinetic centre-of-mass term was divided into two to take into account the anisotropy between effective masses, and added to an anisotropic version of the Rytova-Keldysh potential, for which we found an approximated form. With the aid of this effective Hamiltonian, we calculated the ground state excitonic energy ($E_{\bigcirc} \approx -24$ meV) and wavefunction

in a free-standing sheet of s-Se, using variational methods. We also obtained an unconventional spatial extension of the wavefunction, which covers hundreds of unit cells. To our knowledge, these calculations represent the first study of excitonic properties in square selenene, providing an initial step in the determination of its potential for optical and optoelectronic applications.

In the rest of this chapter, we comment on the limitations of our work, possible improvements, and future directions.

First, the use of hybrid functionals, such as HSE06 or PBE0, is expected to yield more accurate electronic dispersions, at the expense of a higher computational cost. The use of *ab initio* methods to calculate the 2D polarizabilities, and subsequently the screening lengths, would allow for cross-checking with the values from the effective formula. This is particularly relevant, as the screening length in the $||$-direction was found to significantly exceed typical values for 2D semiconductors.

Second, the role of PAOFLOW could be expanded. The logical step would be to use Eq.(3.12) on the Hamiltonian from PAOFLOW to calculate the screening lengths. This would give another point of comparison for the effective lengths obtained from our effective method, and eventually from *ab initio* calculations. Furthermore, the spin-texture in reciprocal space can also be obtained using PAOFLOW, allowing comparison with the spin patterns we obtained from Quantum ESPRESSO.

The third category of improvement is focused on our treatment of excitons. A first step would be to include Eq.(4.5), or at least its angular part, numerically in the minimisation process of the variational method. While this would significantly increase the computational cost, it would also allow for a direct comparison with the values obtained under the use of the approximated potential. We note that the form of the integrals in Eq.(4.5) can be written as Hankel transforms, which could allow the use of specialised software to compute them. It would also be interesting to remove anisotropy from different parts of our treatment, i.e, from the centre-of-mass Hamiltonian or the modified Rytova-Keldysh potential, and analyse how it would affect the excitonic properties. Additionally, the inclusion of surrounding media is easily implementable, and the effects could also be studied. Moreover, the calculation of higher energy excitonic states is feasible by considering more complex trial wavefunctions.

As a possible direction, employing more sophisticated treatments of excitonic properties, such as Wannier-based approaches (WanTiBEXOS[75]) and the use of the Bethe-Salpeter equation on top of GW calculations, would provide rigorous benchmarks against which our variational results could be compared.

Bibliography

[1] Lede Xian, Alejandro Pérez Paz, Elisabeth Bianco, Pulickel M Ajayan, and Angel Rubio. Square selenene and tellurene: novel group vi elemental 2d materials with nontrivial topological properties. *2D Materials*, 4(4):041003, 2017.

[2] Ziyuan Lin, Cong Wang, and Yang Chai. Emerging group-vi elemental 2d materials: Preparations, properties, and device applications. *Small*, 16(41):2003319, 2020.

[3] Zhibin Gao, Gang Liu, and Jie Ren. High thermoelectric performance in two-dimensional tellurium: An ab initio study. *ACS Applied Materials & Interfaces*, 10(47):40702–40709, Nov 2018.

[4] Raghottam M Sattigeri and Prafulla K Jha. Functionalized tellurene; a candidate large-gap 2D topological insulator. *J Phys Condens Matter*, 34(8), 2021.

[5] Gang Liu, Zhibin Gao, Guo-Ling Li, and Hui Wang. Abnormally low thermal conductivity of 2d selenene: An ab initio study. *Journal of Applied Physics*, 127(6):065103, 2020.

[6] Zhendong Chen, Yuefang Hu, Ziming Zhu, and Wei Zhang. Tunable dirac cones in single-layer selenium. *New Journal of Physics*, 22(9):093055, sep 2020.

[7] Høgni C. Kamban, Thomas G. Pedersen, and Nuno M. R. Peres. Anisotropic stark shift, field-induced dissociation, and electroabsorption of excitons in phosphorene. *Physical Review B*, 102(11), 2020.

[8] Chensheng Lin, Wendan Cheng, Guoliang Chai, and Hao Zhang. Thermoelectric properties of two-dimensional selenene and tellurene from group-vi elements. *Phys. Chem. Chem. Phys.*, 20:24250–24256, 2018.

[9] K. S. Novoselov, A. K. Geim, S. V. Morozov, D. Jiang, Y. Zhang, S. V. Dubonos, I. V. Grigorieva, and A. A. Firsov. Electric field effect in atomically thin carbon films. *Science*, 306(5696):666–669, 2004.

[10] N. Stander, B. Huard, and D. Goldhaber-Gordon. Evidence for klein tunneling in graphene $p{-}n$ junctions. *Phys. Rev. Lett.*, 102:026807, 2009.

[11] Changgu Lee, Xiaoding Wei, Jeffrey Kysar, and James Hone. Measurement of the elastic properties and intrinsic strength of monolayer graphene. *Science (New York, N.Y.)*, 321:385–8, 07 2008.

[12] Ke Cao, Shizhe Feng, Ying Han, Libo Gao, Thuc Hue Ly, Zhiping Xu, and Yang Lu. Elastic straining of free-standing monolayer graphene. *Nature Communications*, 11(1):284, Jan 2020.

[13] Xiangfeng Duan and Hua Zhang. Introduction: Two-dimensional layered transition metal dichalcogenides. *Chemical Reviews*, 124(19):10619–10622, Oct 2024.

[14] Alessandro Molle and Carlo Grazianetti, editors. *Xenes: 2D Synthetic Materials Beyond Graphene*. Woodhead Publishing Series in Electronic and Optical Materials. Woodhead Publishing, Elsevier, London, UK, 2022.

[15] Ying Jiang, Junchao Lao, Guangfu Dai, and Zhengqing Ye. Advanced insights on mxenes: Categories, properties, synthesis, and applications in alkali metal ion batteries. *ACS Nano*, 18(22):14050–14084, Jun 2024.

[16] Mohammad Jafar Molaei, Mohammad Younas, and Mashallah Rezakazemi. A comprehensive review on recent advances in two-dimensional (2d) hexagonal boron nitride. *ACS Applied Electronic Materials*, 3(12):5165–5187, Dec 2021.

[17] Meijuan Cheng, Shunqing Wu, Zi-Zhong Zhu, and Guang-Yu Guo. Large second-harmonic generation and linear electro-optic effect in trigonal selenium and tellurium. *Phys. Rev. B*, 100:035202, 2019.

[18] Luz Ramírez-Montes, William López-Pérez, A. González-García, and Rafael González-Hernández. Spin transport and thermoelectric properties in chiral selenium crystals. *Phys. Rev. Mater.*, 8:063601, 2024.

[19] Zi-Yu Chen and Rui Qin. Probing structural chirality of crystals using high-order harmonic generation in solids. *Phys. Rev. A*, 101:053423, 2020.

[20] Minsu Kim, Dabin Park, and Jooheon Kim. A review on recent selenium- and tellurium-based thermoelectric materials and chalcogenide/organic flexible thermoelectric applications. *Materials Chemistry and Physics*, 337:130571, 2025.

[21] D. Royer and E. Dieulesaint. Elastic and piezoelectric constants of trigonal selenium and tellurium crystals. *Journal of Applied Physics*, 50(6):4042–4045, 1979.

[22] A. V. Shibaeva. Piezoelectric effect in polycrystalline selenium. *Soviet Physics Journal*, 8(6):23–25, Nov 1965.

[23] Tae Il Lee, Sangmin Lee, Eungkyu Lee, Sungwoo Sohn, Yean Lee, Sujeong Lee, Geondae Moon, Dohyang Kim, Youn Sang Kim, Jae Min Myoung, and Zhong Lin Wang. High-power density piezoelectric energy harvesting using radially strained ultrathin trigonal tellurium nanowire assembly. *Advanced Materials*, 25(21):2920–2925, 2013.

[24] J.P. Hermann, G. Quentin, and J.M. Thuillier. Determination of the d14 piezoelectric coefficient of tellurium. *Solid State Communications*, 7(1):161–163, 1969.

[25] Peng Liu, Yurong Ma, Weiwei Cai, Zhenzhong Wang, Jian Wang, Limin Qi, and Dongmin Chen. Photoconductivity of single-crystalline selenium nanotubes. *Nanotechnology*, 18(20):205704, apr 2007.

[26] Jian-Wei Liu, Jian-Hua Zhu, Chuan-Ling Zhang, Hai-Wei Liang, and Shu-Hong Yu. Mesostructured assemblies of ultrathin superlong tellurium nanowires and their photoconductivity. *Journal of the American Chemical Society*, 132(26):8945–8952, Jul 2010.

[27] National Minerals Information Center. Selenium and tellurium statistics and information, 2025. Available online :https://www.usgs.gov/centers/national-minerals-information-center/selenium-and-tellurium-statistics-and-information.

[28] Ricardo A. Marques Lameirinhas, João Paulo N. Torres, and João P. de Melo Cunha. A photovoltaic technology review: History, fundamentals and applications. *Energies*, 15(5), 2022.

[29] W. G. Adams and R. E. Day. The action of light on selenium. *Philosophical Transactions of the Royal Society of London*, 167:313–349, 1877.

[30] Chao Liu, Tao Hu, Yabei Wu, Heng Gao, Yali Yang, and Wei Ren. 2d selenium allotropes from first principles and swarm intelligence. *Journal of Physics: Condensed Matter*, 31(23):235702, 2019.

[31] Jochen Heyd, Gustavo E. Scuseria, and Matthias Ernzerhof. Hybrid functionals based on a screened coulomb potential. *The Journal of Chemical Physics*, 118(18):8207–8215, 2003.

[32] Dan Wang, Li-Ming Tang, Xing-Xing Jiang, Jie-Yao Tan, Meng-Dong He, Xin-Jun Wang, and Ke-Qiu Chen. High bipolar conductivity and robust in-plane spontaneous electric polarization in selenene. *Advanced Electronic Materials*, 5(2):1800475, 2019.

[33] A. N. Rudenko, S. Brener, and M. I. Katsnelson. Intrinsic charge carrier mobility in single-layer black phosphorus. *Phys. Rev. Lett.*, 116:246401, 2016.

[34] Jingkai Qin, Gang Qiu, Jie Jian, Hong Zhou, Lingming Yang, Adam Charnas, Dmitry Y. Zemlyanov, Cheng-Yan Xu, Xianfan Xu, Wenzhuo Wu, Haiyan Wang, and Peide D. Ye. Controlled growth of a large-size 2d selenium nanosheet and its electronic and optoelectronic applications. *ACS Nano*, 11(10):10222–10229, Oct 2017.

[35] John P. Perdew, Kieron Burke, and Matthias Ernzerhof. Generalized gradient approximation made simple. *Phys. Rev. Lett.*, 77:3865–3868, 1996.

[36] Showkat Hassan Mir, Vivek Kumar Yadav, and Jayant Kumar Singh. Recent advances in the carrier mobility of two-dimensional materials: A theoretical perspective. *ACS Omega*, 5(24):14203–14211, Jun 2020.

[37] Yuhong Zhou, Kan Luo, Xian-Hu Zha, Zhen Liu, Xiaojing Bai, Qing Huang, Zhansheng Guo, Cheng-Te Lin, and Shiyu Du. Electronic and transport properties of ti2co2 mxene nanoribbons. *The Journal of Physical Chemistry C*, 120, 07 2016.

[38] Thomas Mueller and Ermin Malic. Exciton physics and device application of two-dimensional transition metal dichalcogenide semiconductors. *npj 2D Materials and Applications*, 2(1):29, Sep 2018.

[39] Eesha Andharia, Thaneshwor P. Kaloni, Gregory J. Salamo, Shui-Qing Yu, Hugh O. H. Churchill, and Salvador Barraza-Lopez. Exfoliation energy, quasiparticle band structure, and excitonic properties of selenium and tellurium atomic chains. *Phys. Rev. B*, 98:035420, 2018.

[40] Project Jupyter. Jupyter notebook, 2023. Available online: https://jupyter.org/.

[41] Anaconda, Inc. Anaconda software distribution, 2023. Available online: https://www.anaconda.com/.

[42] Wolfram Research, Inc. Mathematica, Version 14.3. Champaign, IL, 2025.

[43] David Nichols. Coloring for colorblindness, 2025. Available online: https://davidmathlogic.com/colorblind/.

[44] Paolo Giannozzi, Stefano Baroni, Nicola Bonini, Matteo Calandra, Roberto Car, Carlo Cavazzoni, Davide Ceresoli, Guido L Chiarotti, Matteo Cococcioni, Ismaila Dabo, Andrea Dal Corso, Stefano

de Gironcoli, Stefano Fabris, Guido Fratesi, Ralph Gebauer, Uwe Gerstmann, Christos Gougoussis, Anton Kokalj, Michele Lazzeri, Layla Martin-Samos, Nicola Marzari, Francesco Mauri, Riccardo Mazzarello, Stefano Paolini, Alfredo Pasquarello, Lorenzo Paulatto, Carlo Sbraccia, Sandro Scandolo, Gabriele Sclauzero, Ari P Seitsonen, Alexander Smogunov, Paolo Umari, and Renata M Wentzcovitch. Quantum espresso: a modular and open-source software project for quantum simulations of materials. *Journal of Physics: Condensed Matter*, 21(39):395502 (19pp), 2009.

[45] P Giannozzi, O Andreussi, T Brumme, O Bunau, M Buongiorno Nardelli, M Calandra, R Car, C Cavazzoni, D Ceresoli, M Cococcioni, N Colonna, I Carnimeo, A Dal Corso, S de Gironcoli, P Delugas, R A DiStasio Jr, A Ferretti, A Floris, G Fratesi, G Fugallo, R Gebauer, U Gerstmann, F Giustino, T Gorni, J Jia, M Kawamura, H-Y Ko, A Kokalj, E Küçükbenli, M Lazzeri, M Marsili, N Marzari, F Mauri, N L Nguyen, H-V Nguyen, A Otero de-la Roza, L Paulatto, S Poncé, D Rocca, R Sabatini, B Santra, M Schlipf, A P Seitsonen, A Smogunov, I Timrov, T Thonhauser, P Umari, N Vast, X Wu, and S Baroni. Advanced capabilities for materials modelling with quantum espresso. *Journal of Physics: Condensed Matter*, 29(46):465901, 2017.

[46] Hendrik J. Monkhorst and James D. Pack. Special points for brillouin-zone integrations. *Phys. Rev. B*, 13:5188–5192, 1976.

[47] Hiren S Patel, Vishnu A Dabhi, and Aditya M Vora. Adverse effect of k-mesh shifting in several crystal systems: An analytical study. *Materials Today: Proceedings*, 57:275–278, 2022. International Symposium on Materials of the Millennium: Emerging Trends and Future Prospects.

[48] Huaqing Huang, Zhirong Liu, Hongbin Zhang, Wenhui Duan, and David Vanderbilt. Emergence of a chern-insulating state from a semi-dirac dispersion. *Phys. Rev. B*, 92:161115, 2015.

[49] A. Manchon, H. C. Koo, J. Nitta, S. M. Frolov, and R. A. Duine. New perspectives for rashba spin–orbit coupling. *Nature Materials*, 14(9):871–882, 2015.

[50] B. Geldiyev, M. Ünzelmann, P. Eck, T. Kißlinger, J. Schusser, T. Figgemeier, P. Kagerer, N. Tezak, M. Krivenkov, A. Varykhalov, A. Fedorov, L. Nicolaï, J. Minár, K. Miyamoto, T. Okuda, K. Shimada, D. Di Sante, G. Sangiovanni, L. Hammer, M. A. Schneider, H. Bentmann, and F. Reinert. Strongly anisotropic spin and orbital rashba effect at a tellurium – noble metal interface. *Phys. Rev. B*, 108:L121107, 2023.

[51] Zhuang Ma, Hongquan Song, Yujie Wang, Chunyan Wang, Wenjie Wang, Heng Yu, Jingwen Jiang, and

Yiguo Xu. Ferroelasticity tuned anisotropic rashba effect and negative poisson's ratio in janus wurtzite monolayer m2xy (m = zn, cd; x, y = s, se, te). *Computational Materials Science*, 246:113511, 2025.

[52] Ya Feng, Qi Jiang, Baojie Feng, Yang Meng, Tao Xu, Wenjing Liu, Xiufu Yang, Masashi Arita, Eike Schwier, Kenya Shimada, Harald Jeschke, Ronny Thomale, Youguo Shi, Xian Wu, Shaozhu Xiao, Shan Qiao, and Shaolong He. Rashba-like spin splitting along three momentum directions in trigonal layered ptbi 2. *Nature Communications*, 10:4765, 10 2019.

[53] Sangmin Lee, Miyoung Kim, and Young-Kyun Kwon. Unconventional hidden rashba effects in two-dimensional inte. *npj 2D Materials and Applications*, 7(1):43, Jun 2023.

[54] Marco Buongiorno Nardelli, Frank T. Cerasoli, Marcio Costa, Stefano Curtarolo, Riccardo De Gennaro, Marco Fornari, Laalitha Liyanage, Andrew R. Supka, and Haihang Wang. Paoflow: A utility to construct and operate on ab initio hamiltonians from the projections of electronic wavefunctions on atomic orbital bases, including characterization of topological materials. *Computational Materials Science*, 143:462–472, 2018.

[55] Haifeng Lang, Shuqing Zhang, and Zhirong Liu. Mobility anisotropy of two-dimensional semiconductors. *Phys. Rev. B*, 94:235306, 2016.

[56] Pierluigi Cudazzo, Ilya V. Tokatly, and Angel Rubio. Dielectric screening in two-dimensional insulators: Implications for excitonic and impurity states in graphane. *Physical Review B*, 84(8), 2011.

[57] T. Tian, D. Scullion, D. Hughes, L. H. Li, C. Shih, J. N. Coleman, M. Chhowalla, and E. J. G. Santos. Electronic polarizability as the fundamental variable in the dielectric properties of two-dimensional materials. *Nano Letters*, 20:841–851, 2019.

[58] Timothy Berkelbach, Mark Hybertsen, and David Reichman. Theory of neutral and charged excitons in monolayer transition metal dichalcogenides. *Physical Review B*, 88, 05 2013.

[59] Pengke Li and Ian Appelbaum. Excitons without effective mass: Biased bilayer graphene. *Physical Review B*, 99(3), 2019.

[60] Zeyu Jiang, Zhirong Liu, Yuanchang Li, and Wenhui Duan. Scaling Universality between Band Gap and Exciton Binding Energy of Two-Dimensional Semiconductors. , 118(26):266401, 2017.

[61] A. S. Rodin, A. Carvalho, and A. H. Castro Neto. Excitons in anisotropic two-dimensional semiconducting crystals. *Phys. Rev. B*, 90:075429, 2014.

[62] S. Rytova. *Moscow Univ. Phys. Bull.*, 22:30, 1967.

[63] L. V. Keldysh. *Sov. J. Exp. Theor. Phys. Lett.*, 29:658, 1979.

[64] Maurício F. C. Martins Quintela and Nuno M. R. Peres. A colloquium on the variational method applied to excitons in 2d materials. *The European Physical Journal B*, 93(12):222, Dec 2020.

[65] Jin-Ho Choi, Ping Cui, Haiping Lan, and Zhenyu Zhang. Linear Scaling of the Exciton Binding Energy versus the Band Gap of Two-Dimensional Materials. , 115(6):066403, 2015.

[66] Mingliang Zhang, Ling-Yi Huang, Xu Zhang, and Gang Lu. Comment on "linear scaling of the exciton binding energy versus the band gap of two-dimensional materials". *Physical Review Letters*, 118(20), 2017.

[67] Linyang Li, Xiaoming Zhang, Xin Chen, and Mingwen Zhao. Giant topological nontrivial band gaps in chloridized gallium bismuthide. *Nano Letters*, 15(2):1296–1301, Feb 2015.

[68] Junwei Liu, Xiaofeng Qian, and Liang Fu. Crystal field effect induced topological crystalline insulators in monolayer iv–vi semiconductors. *Nano Letters*, 15(4):2657–2661, 2015. PMID: 25741907.

[69] Xiaomu Wang, Aaron M. Jones, Kyle L. Seyler, Vy Tran, Yichen Jia, Huan Zhao, Han Wang, Li Yang, Xiaodong Xu, and Fengnian Xia. Highly anisotropic and robust excitons in monolayer black phosphorus. *Nature Nanotechnology*, 10(6):517–521, Jun 2015.

[70] Miguel M. Ugeda, Aaron J. Bradley, Su-Fei Shi, Felipe H. da Jornada, Yi Zhang, Diana Y. Qiu, Wei Ruan, Sung-Kwan Mo, Zahid Hussain, Zhi-Xun Shen, Feng Wang, Steven G. Louie, and Michael F. Crommie. Giant bandgap renormalization and excitonic effects in a monolayer transition metal dichalcogenide semiconductor. *Nature Materials*, 13(12):1091–1095, Dec 2014.

[71] Mateusz Dyksik, Michal Baranowski, Joshua J. P. Thompson, Zhuo Yang, Martha Rivera Medina, Maria Antonietta Loi, Ermin Malic, and Paulina Plochocka. Steric engineering of exciton fine structure in 2d perovskites. *Advanced Energy Materials*, 15(9):2404769, 2025.

[72] Jonas Zipfel, Johannes Holler, Anatolie A. Mitioglu, Mariana V. Ballottin, Philipp Nagler, Andreas V. Stier, Takashi Taniguchi, Kenji Watanabe, Scott A. Crooker, Peter C. M. Christianen, Tobias Korn, and Alexey Chernikov. Spatial extent of the excited exciton states in ws_2 monolayers from diamagnetic shifts. *Phys. Rev. B*, 98:075438, 2018.

[73] Kaigui Zhu, Jianzhong Shi, and Lide Zhang. Preparation and optical absorption of insb microcrystallites embedded in sio2 thin films. *Solid State Communications*, 107(2):79–84, 1998.

[74] J. C. G. Henriques and N. M. R. Peres. Excitons in phosphorene: A semi-analytical perturbative approach. *Phys. Rev. B*, 101:035406, 2020.

[75] Alexandre C. Dias, Julian F.R.V. Silveira, and Fanyao Qu. Wantibexos: A wannier based tight binding code for electronic band structure, excitonic and optoelectronic properties of solids. *Computer Physics Communications*, 285:108636, 2023.

[76] S. Mikhlin. *Integral Equations and Their Applications to Certain Problems in Mechanics, Mathematical Physics and Technology*. Pergamon Press, Oxford, England, 2 edition, 1964.

Part I
Appendices

Appendix A
PAOFLOW

PAOFLOW[54] is a software tool developed to efficiently post-process the output from conventional first-principles electronic structure plane-wave pseudopotential calculations, such as those obtained from Quantum ESPRESSO. It allows for the calculation of various quantities, such as optical conductivities, Berry curvature, and anomalous and spin Hall conductivities, from interpolated band structures and density of states. The starting point consists of generating finite-basis real-space Hamiltonians - $H(\mathbf{R})$ - from the projection of the first principles plane-wave pseudopotential wavefunctions onto pseudo-atomic orbitals, hence the name **PAO**FLOW.

In this thesis, we employed PAOFLOW to generate a real-space tight-binding Hamiltonian for square selenene from the data obtained from Quantum ESPRESSO. Firstly, we performed a self-consistent field calculation (SCF), followed by a non-consistent field calculation (NSCF) with a Monkhorst-Pack grid of 13×13×1 and a cutoff energy for the Kohn-Sham orbitals of 90 Ry. The final computation in *QE* consists of using **projwfc.x** to project the calculated wavefunctions onto orthogonalised atomic wavefunctions. The input provided to PAOFLOW is stored in two files: "atomic_proj.xml" and "data-file-schema.xml". From here, we use PAOFLOW to obtain the real-space Hamiltonian.

Some quantities are crucial for understanding the format in which the real-space Hamiltonian is stored. First is the basis size, which corresponds to the number of states per unit cell, labelled M, as well as the size $M \times M$ of the Hamiltonian in matrix representation. The number of states per unit cell is dictated by the pseudopotential. Secondly, the number of k-points used in the NSCF calculation: $n_1 \times n_2 \times n_3 = N_k$. These points translate to unit cells in real space, one central and $\frac{n_i - 1}{2}$ cells in each direction. The hopping parameters, between states, are calculated between the central unit cell and the N_k-1 surrounding cells, as well as intra-cell hoppings. This gives a total of $N_k \times N^2$ terms. For a more detailed explanation on the computation of the hoppings, see the work done by Buongiorno *et al.*[54].

The file that PAOFLOW outputs is structured in the following way:

$$\begin{array}{cccccc} M & N_k & & & & \\ a_1 & a_2 & a_3 & i & j & Re\left(t^{ij}_{a_1 a_2 a_3}\right) \quad \mathrm{Im}\left(t^{ij}_{a_1 a_2 a_3}\right) \\ & & & & \vdots & \end{array} \quad ,$$

where $t^{ij}_{a_1 a_2 a_3}$ is the hopping parameter between state i in the central unit cell - (0,0,0) - and state j in the cell (a_1,a_2,a_3). For square selenene, there are 2 atoms per unit cell, with 4 orbitals each (4s, 4p_x, 4p_y, and 4p_z) and two spin states, giving M=16 states per unit cell. Our performed NSCF run used a 13×13×1 MP grid, which gives a total of 169 unit cells in real space. The resulting Hamiltonian, which consists of 169(16)^2=43264 hoppings, gives the band structure, after a Fourier transform and diagonalization, shown in Fig.23. For comparison, we also plot the corresponding DFT band structure.

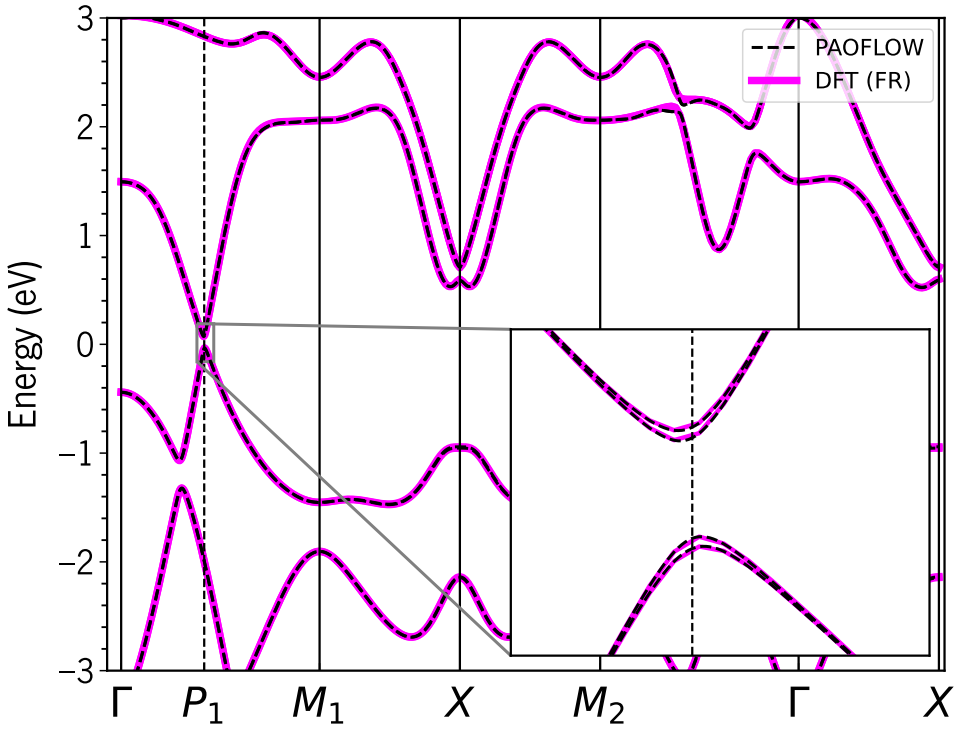


Figure 23: Comparison of the band structures obtained from DFT (fully-relativistic), and PAOFLOW's real space Hamiltonian.

We obtain an almost exact description of the bands, even the fine details like the additional splitting near P_1. Apart from the hopping parameters, PAOFLOW also outputs a projectability vector, which gives the projectability value for each band. This quantity measures how well a Kohn-Sham Bloch state is represented by the chosen PAO basis set[54]. The projectability goes from 0 to 1, with 1 indicating that the KS Bloch state can be perfectly represented. This quantity tends to be very small for the highest bands included in the DFT calculations, so it is good practice to include extra bands above the relevant ones.

Appendix B
Effective Model: Anisotropic Rashba spin-orbit coupling term

We started with the model Hamiltonian, where the Rashba term is isotropic

$$H_{\text{eff}} = H_{k\cdot p} + H_{\text{SO}} + H_{\text{R}}, \tag{B.1}$$

with

$$H_{\text{R}} = \alpha_{\text{R}} \left(\sigma_x \otimes s_y - \sigma_y \otimes s_x \right), \tag{B.2}$$

where α_{R} is the Rashba constant,s_i are the Pauli matrices associated with the spin degree of freedom, and σ_i are the Pauli matrices associated with the sub-lattice degree of freedom.

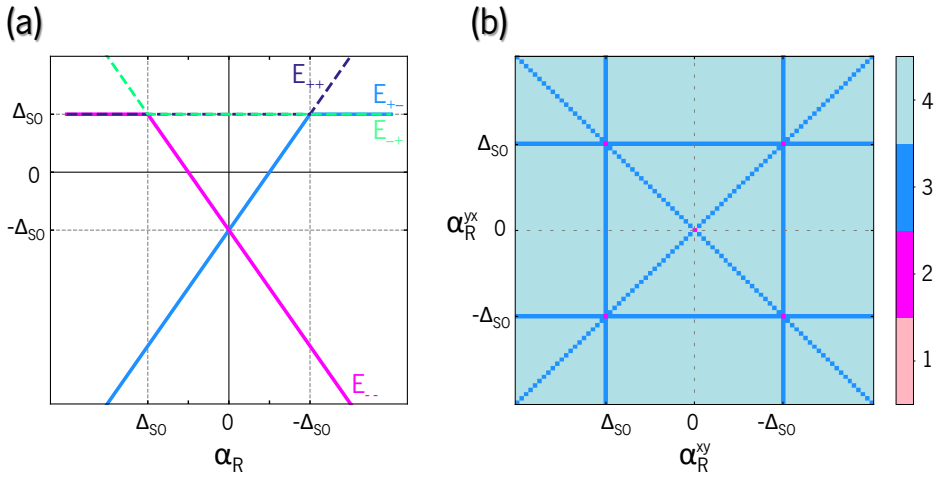


Figure 24: (a) Eigenvalues of the Rashba Hamiltonian in function of the Rashba parameter α_{R}.(b) Number of distinct eigenvalues of the anisotropic Rashba Hamiltonian in terms of the Rashba parameters α_{R}^{xy} and α_{R}^{yx}.

We then considered the eigenvalues as $\mathbf{q} \to \mathbf{0}$, which can be compactly represented as

$$E_{s_1 s_2} = s_1 \alpha_{\text{R}} + s_2 \left| \Delta_{\text{SO}} - \alpha_{\text{R}} \right|, \qquad s_1, s_2 \in \{+1, -1\} \tag{B.3}$$

There are four regions depending if $|\alpha_R| \lessgtr |\Delta_{SO}|$, as shown in Fig.24(a), however, there is no value of α_R where we get four distinct eigenvalues. This led us to consider an anisotropic version of the Rashba term, given by

$$H_R^{ani}(\alpha_R^{xy}, \alpha_R^{yx}) = \alpha_R^{xy}(\sigma_x \otimes s_y) - \alpha_R^{yx}(\sigma_y \otimes s_x). \tag{B.4}$$

We calculated the number of distinct eigenvalues produced by the total Hamiltonian at $\mathbf{q}$=$\mathbf{0}$ in function of the parameters $\alpha_R^{xy}, \alpha_R^{yx}$ and show the result in Fig.24(b). It is clear that H_R^{ani} can produce 4 distinct eigenvalues at P_1.

Appendix C
Anisotropic Poisson equation

In this appendix, we replicate the derivation of the interaction energy between two charged particles inside an anisotropic 2D semiconductor done by Kamban et al.[7]. The derivation follows closely theirs and adds some in-between steps for more clarity. We start with the Poisson equation for the potential between two charges, Q and Q', located at (x,y,z) and (0,0,z') respectively

$$\nabla \cdot [\boldsymbol{\epsilon} \cdot \nabla V(x, y, z, z')] = -QQ' \delta(x)\delta(y)\delta(z - z'), \tag{C.1}$$

where $\boldsymbol{\epsilon}$ is the dielectric tensor, which we considered to be anisotropic, diagonal, and only varies along the z direction

$$\epsilon_{ij}(x, y, z) \rightarrow \epsilon_{ii}(z), \tag{C.2}$$

which allows us to write the Poisson equation as

$$\epsilon_{xx}\frac{\partial^2 V}{\partial x^2} + \epsilon_{yy}\frac{\partial^2 V}{\partial y^2} + \frac{\partial}{\partial z}\left(\epsilon_{zz}(z)\frac{\partial V}{\partial z}\right) = -QQ'\delta(x)\delta(y)\delta(z - z'). \tag{C.3}$$

The inverse Fourier transform of the potential is given by

$$V(x, y, z, z') = \frac{1}{(2\pi)^2}\int_{-\infty}^{\infty}\int_{-\infty}^{\infty}\tilde{\mathrm{V}}(z, z'; q_x, q_y)e^{i(q_x x + q_y y)}dq_x dq_y. \tag{C.4}$$

Substituting this expression in Eq. (C.3) yields

$$\left[-\epsilon_{xx}q_x^2 - \epsilon_{yy}q_y^2 + \frac{\partial}{\partial z}\left(\epsilon_{zz}(z)\frac{\partial}{\partial z}\right)\right]\tilde{\mathrm{V}}(z, z'; q_x, q_y) = QQ'\delta(z - z'). \tag{C.5}$$

We now assume that the dielectric tensor is piecewise constant

$$\epsilon_{ii}(z) = \begin{cases} \epsilon_{ii}^{(a)}, & z > \frac{d}{2} \\ \epsilon_{ii}, & -\frac{d}{2} < z < \frac{d}{2}, \\ \epsilon_{ii}^{(b)}, & z < -\frac{d}{2} \end{cases} \tag{C.6}$$

where a and b stand for "above" and "below", respectively, and search for solutions of the form

$$\tilde{\mathrm{V}}^{\left(\begin{smallmatrix}\mathrm{a}\\ \mathrm{s}\\ \mathrm{b}\end{smallmatrix}\right)}(z,z';q_x,q_y)=\frac{2\pi QQ'}{q}\begin{cases}A_1e^{-q_\mathrm{a}z}, z>\frac{d}{2}\\ A_2e^{qz}+B_2e^{-qz}+\frac{1}{\epsilon_{zz}}e^{-q|z-z'|}, -\frac{d}{2}<z<\frac{d}{2}\\ B_3e^{q_\mathrm{b}z}, z<-\frac{d}{2}\end{cases}, \tag{C.7}$$

where s stands for "sheet" and q_i has the form

$$q_i=\sqrt{\frac{\epsilon_{zz}^{(i)}q_x^2+\epsilon_{zz}^{(i)}q_y^2}{\epsilon_{zz}^{(i)}}}. \tag{C.8}$$

The derivative along z is given by

$$\frac{\partial\tilde{\mathrm{V}}^{\left(\begin{smallmatrix}\mathrm{a}\\ \mathrm{s}\\ \mathrm{b}\end{smallmatrix}\right)}}{\partial z}=\frac{2\pi QQ'}{q}\begin{cases}-q_\mathrm{a}A_1e^{-q_\mathrm{a}z}, z>\frac{d}{2}\\ -q\left(A_2e^{qz}-B_2e^{-qz}+\frac{\mathrm{sgn}(z-z')}{\epsilon_{zz}}e^{-q|z-z'|}\right), -\frac{d}{2}<z<\frac{d}{2}\\ q_\mathrm{b}B_3e^{q_\mathrm{b}z}, z<-\frac{d}{2}\end{cases}. \tag{C.9}$$

The Fourier components satisfy the boundary conditions for the electric potential

$$\begin{aligned}&\tilde{\mathrm{V}}^{\left(\begin{smallmatrix}\mathrm{a}\\ \mathrm{b}\end{smallmatrix}\right)}\left(\pm\tfrac{d}{2},z';q_x,q_y\right)=\tilde{\mathrm{V}}^{\mathrm{s}}\left(\pm\tfrac{d}{2},z';q_x,q_y\right)\ \text{(i)}\\ &\epsilon_z^{\left(\begin{smallmatrix}\mathrm{a}\\ \mathrm{b}\end{smallmatrix}\right)}\frac{\partial\tilde{\mathrm{V}}^{\left(\begin{smallmatrix}\mathrm{a}\\ \mathrm{b}\end{smallmatrix}\right)}}{\partial z}\left(z,z';q_x,q_y\right)\Big|_{z=\pm\frac{d}{2}}=\epsilon_{zz}^{\mathrm{s}}\frac{\partial\tilde{\mathrm{V}}^{\mathrm{s}}}{\partial z}\left(z,z';q_x,q_y\right)\Big|_{z=\pm\frac{d}{2}}\ \text{(iii)}\end{aligned}\quad\begin{matrix}\\ \text{(ii)}\\ \\ \text{(iv)}\end{matrix}. \tag{C.10}$$

These four boundary conditions lead to a system of four equations for the parameters A_1,A_2,B_2, and B_3

$$\begin{cases}A_1e^{-q_\mathrm{a}\frac{d}{2}}-A_2e^{-q\frac{d}{2}}-B_2e^{q\frac{d}{2}}-\frac{2}{\epsilon_{zz}}e^{-q|\frac{d}{2}-z'|}=0\\ B_3e^{-q_\mathrm{b}\frac{d}{2}}-A_2e^{q\frac{d}{2}}-B_2e^{-q\frac{d}{2}}-\frac{1}{\epsilon_{zz}}e^{-q|\frac{d}{2}+z'|}=0\\ -\epsilon_{zz}^{\mathrm{a}}q_\mathrm{a}A_1e^{-q_\mathrm{a}\frac{d}{2}}+\epsilon_{zz}q\left(A_2e^{-q\frac{d}{2}}-B_2e^{q\frac{d}{2}}-\frac{\mathrm{sgn}\left(\frac{d}{2}-z'\right)}{\epsilon_{zz}}e^{-q|\frac{d}{2}+z'|}\right)=0\\ -\epsilon_{zz}^{\mathrm{b}}q_\mathrm{b}B_3e^{-q_\mathrm{b}\frac{d}{2}}+\epsilon_{zz}q\left(A_2e^{q\frac{d}{2}}-B_2e^{-q\frac{d}{2}}-\frac{\mathrm{sgn}\left(-\frac{d}{2}-z'\right)}{\epsilon_{zz}}e^{-q|\frac{d}{2}-z'|}\right)=0\end{cases}. \tag{C.11}$$

Considering these boundary conditions, placing both charges inside the sheet ($z=z'=0$) and switching to polar coordinates, Kamban *et al.*[7] found

$$\tilde{\mathrm{V}}(0,0;q,\phi)=\frac{\tilde{\mathrm{V}}_0(q)}{\epsilon_{\mathrm{eff}}(q,\phi)}, \tag{C.12}$$

were they retrieved the bare interaction - $\tilde{\mathrm{V}}_0(q)=2\pi QQ'/q$ - and obtained an effective dielectric function given by

$$\epsilon_{\text{eff}}(q,\phi) = \frac{g^2(g_a+g_b)\cosh\left(\frac{dq}{\epsilon_{zz}}g\right) + g(g^2+g_ag_b)\sinh\left(\frac{dq}{\epsilon_{zz}}g\right)}{g^2 - g_ag_b(g^2+g_ag_b)\cosh\left(\frac{dq}{\epsilon_{zz}}g\right) + g(g_a+g_b)\sinh\left(\frac{dq}{\epsilon_{zz}}g\right)}, \tag{C.13}$$

with

$$g_i(\phi) = \sqrt{\epsilon^i_{zz}\left[\epsilon^i_{xx}\cos^2\phi + \epsilon^i_{yy}\sin^2\phi\right]}. \tag{C.14}$$

Next, we consider the surrounding media to be isotropic in the x and y directions, i.e, $\epsilon^{(a/b)}_{xx} = \epsilon^{(a/b)}_{yy} \equiv \epsilon^{(a/b)}$ and expand the effective dielectric function until first order in q

$$\begin{aligned}
\epsilon^{(1)}_{\text{eff}}(q,\phi) &= \epsilon_{\text{eff}}(0,\phi) + q\frac{\partial\epsilon_{\text{eff}}}{\partial q}\bigg|_{q=0} + O(q^2) \\
&= \frac{g^2(g_a+g_b)\cosh(0) + g(g^2+g_ag_b)\sinh(0)}{g^2 - g_ag_b(g^2+g_ag_b)\cosh(0) + g(g_a+g_b)\sinh(0)} \\
&\quad + q\frac{2d(g^2+g_ag_b) - d(g_a+g_b)^2}{4\epsilon_{zz}} + O(q^2) \\
&= \frac{g^2(g_a+g_b)}{g^2 - g_ag_b + g^2 + g_ag_b} + q\frac{\mathrm{d}\left(2g^2 - g_a^2 - g_b^2\right)}{4\epsilon_{zz}} + O(q^2) \\
&= \underbrace{\frac{g_a+g_b}{2}}_{\equiv\kappa} + q\underbrace{\frac{d\left[2\epsilon_{zz}\left(\epsilon_{xx}\cos^2\phi + \epsilon_{yy}\sin^2\phi\right) - \epsilon^{(a)}\epsilon^{(a)}_{zz} - \epsilon^{(b)}\epsilon^{(b)}_{zz}\right]}{4\epsilon_{zz}}}_{\equiv r_0(\phi)} + O(q^2) \\
&= \kappa + r_0(\phi)\,q + O(q^2) \\
&= \kappa + \underbrace{\frac{d\epsilon_{xx}}{2}}_{\equiv r_{0x}}\cos^2\phi\, q + \underbrace{\frac{d\epsilon_{yy}}{2}}_{\equiv r_{0y}}\sin^2\phi\, q \underbrace{- \frac{d}{4\epsilon_{zz}}\left(g_a^2+g_b^2\right)}_{\equiv a} q \\
&= \kappa + r_{0x}\cos^2\phi q + r_{0y}\left(1-\cos^2\phi\right)q + aq \\
&= \underbrace{\kappa + (a + r_{0y})q}_{\equiv\alpha(q)} - \left(r_{0y} - r_{0x}\right)q\cos^2\phi \\
&= \alpha(q)\left[1 - \underbrace{\frac{(r_{0y}-r_{0x})q}{\alpha(q)}}_{\equiv\gamma^2(q)}\cos^2\phi\right] \\
&= \alpha(q)\left[1 - \gamma^2(q)\cos^2\phi\right].
\end{aligned} \tag{C.15}$$

It is useful to express $1/\epsilon^{(1)}_{\text{eff}}$ as a Fourier series since it allows us, further down the line, to express the interaction energy as integrals with integration kernels proportional to Bessel functions of the first kind. The equation obtained by Kamban et al.[7], using the methods from the book by Mikhlin[76], is

$$\frac{1}{\epsilon^{(1)}_{\text{eff}}} = \frac{1}{\alpha\sqrt{1-\gamma^2}}\left[1 + 2\sum_{k=1}^{\infty}\left(\frac{\gamma}{1+\sqrt{1-\gamma^2}}\right)^{2k}\cos(2k\phi)\right], \tag{C.16}$$

which allows us to express the first-order approximation of the interaction energy as

$$\begin{aligned} V(0,0;x,y) &= \frac{1}{(2\pi)^2}\int_{-\infty}^{\infty}\int_{-\infty}^{\infty}\tilde{V}(0,0;q_x,q_y)e^{i\left(q_x x+q_y y\right)}dq_x dq_y \\ &= \frac{1}{(2\pi)^2}\int_0^{2\pi}\int_0^{\infty}\tilde{V}(0,0;q,\phi)e^{iq(x\cos\phi+y\sin\phi)}q\,dqd\phi \Leftrightarrow \\ \Leftrightarrow V(0,0;r,\theta) &\approx \frac{QQ'}{2\pi}\int_0^{2\pi}\int_0^{\infty}\frac{e^{iqr\cos(\theta-\phi)}}{\epsilon_{\text{eff}}^{(1)}}dqd\phi \\ &= \frac{QQ'}{2\pi}\int_0^{2\pi}\int_0^{\infty}\frac{e^{iqr\cos(\theta-\phi)}}{\alpha\sqrt{1-\gamma^2}}\left[1+2\sum_{k=1}^{\infty}\left(\frac{\gamma}{1+\sqrt{1-\gamma^2}}\right)^{2k}\cos\left(2k\phi\right)\right]dqd\theta. \end{aligned} \tag{C.17}$$

We now express the following integral using Bessel functions of the first kind

$$\begin{aligned} I_k &\equiv \int_0^{2\pi} e^{iqr\cos(\phi-\theta)}\cos\left(2k\phi\right)d\phi \\ &= \int_0^{2\pi} e^{iqr\cos u}\cos\left[2k\left(u+\theta\right)\right]du \\ &= 2\cos\left(2k\theta\right)\underbrace{\int_0^{\pi} e^{iqr\cos(u)}\cos\left(2ku\right)du}_{=(i)^{2k}\pi J_{2k}(qr)} + \sin\left(2k\theta\right)\cancelto{0}{\int_0^{2\pi} e^{iqr\cos(u)}\sin\left(2ku\right)du} \qquad \text{(C.18)} \\ &= 2\pi\cos\left(2k\theta\right)(-1)^k J_{2k}(qr), \qquad \text{(C.19)} \end{aligned}$$

where we used Bessel's integrals

$$J_n(z) = \frac{i^{-n}}{\pi}\int_0^{\pi} e^{iz\cos(\theta)}\cos\left(n\theta\right)d\theta, \tag{C.20}$$

and evaluated the second integral in Eq.(C.18) to be zero by expanding the complex exponential using the Jacobi-Anger identity, then rewriting $\sin(2ku)$ using Euler's formula, which yields

$$\begin{aligned} \int_0^{2\pi} e^{iqr\cos(u)}\sin\left(2ku\right)du &= \sum_{n=-\infty}^{\infty}\frac{i^{n-1}}{2}J_n(qr)\left[\int_0^{2\pi}e^{i(n+2k)u}du - \int_0^{2\pi}e^{i(n-2k)u}du\right] \\ &= \pi\sum_{n=-\infty}^{\infty} i^{n-1}J_n(qr)(\delta_{n,-2k}-\delta_{n,2k}) \\ &= \pi\left(i^{-2k-1}J_{-2k}(qr) - i^{2k-1}J_{2k}(qr)\right) \end{aligned}$$

$$= \pi J_{2k}(qr)\left(i^{-2k-1}\cancel{(-1)^{2k}}^{1} - i^{2k-1}\right)$$
$$= \pi J_{2k}(qr)\cancel{\left(i^{-2k-1} - i^{2k-1}\right)}^{0}$$
$$= 0.$$

With this we rewrite Eq.(C.17) as

$$V^{(1)}(r,\theta) = \frac{QQ'}{2\pi}\int_0^\infty \frac{2\pi}{\alpha\sqrt{1-\gamma^2}}\left[J_0(qr) + 2\sum_{k=1}^{\infty}(-1)^k\left(\frac{\gamma}{1+\sqrt{1-\gamma^2}}\right)^{2k} J_{2k}(qr)\cos(2k\theta)\right]dq, \tag{C.21}$$

where the first term inside the square brackets was trivially evaluated using Bessel's integrals. Typically $a << r_{0y}$, which implies that $\alpha \approx \kappa + r_{0y}q$. We define the following dielectric functions

$$\epsilon_X = \kappa + r_{0x}q \tag{C.22}$$
$$\epsilon_Y = \kappa + r_{0y}q, \tag{C.23}$$

which entails that $\epsilon_Y = \alpha$ and $\gamma^2 = \frac{\epsilon_Y - \epsilon_X}{\epsilon_Y}$. Using these quantities, we rewrite the prefactors containing α and γ

$$\frac{1}{\alpha\sqrt{1-\gamma^2}} = \frac{1}{\sqrt{\epsilon_X\epsilon_Y}}, \tag{C.24}$$

and

$$\frac{\gamma}{1+\sqrt{1-\gamma^2}} = \frac{\sqrt{\frac{\epsilon_Y-\epsilon_X}{\epsilon_Y}}}{1+\sqrt{1-\frac{(\epsilon_Y+\epsilon_X)}{\epsilon_Y}}}$$
$$= \frac{\sqrt{\epsilon_Y-\epsilon_X}}{\sqrt{\epsilon_X}+\sqrt{\epsilon_Y}}$$
$$= \left(\frac{\sqrt{\epsilon_Y}-\sqrt{\epsilon_X}}{\sqrt{\epsilon_X}+\sqrt{\epsilon_Y}}\right)^{\frac{1}{2}}. \tag{C.25}$$

The final first order interaction energy is then given by [1]

$$V^{(1)}(r,\theta) = \frac{QQ'}{2\pi}\int_0^\infty \frac{2\pi}{\sqrt{\epsilon_X\epsilon_Y}}\left[J_0(qr) + 2\sum_{k=1}^{\infty}\left(\frac{\sqrt{\epsilon_X}-\sqrt{\epsilon_Y}}{\sqrt{\epsilon_X}+\sqrt{\epsilon_Y}}\right)^k J_{2k}(qr)\cos(2k\theta)\right]dq. \tag{C.26}$$

[1] The $(-1)^k$ factor that came from the integrals in θ switches the order of ϵ_X and ϵ_Y inside the prefactor of $J_{2k}(qr)$.

This work was supported by the Fundação para a Ciência e a Tecnologia (FCT-Portugal) through project PTDC/FIS-MAC/2045/2021.